

# Reddening and Star Formation in Starburst Galaxies.

Daniela Calzetti<sup>1</sup>

Space Telescope Science Institute, 3700 San Martin Dr., Baltimore, MD 21218, USA

Received July 22, 1996;    accepted October 17, 1996

To appear in the *Astronomical Journal*

arXiv:astro-ph/9610184v1 23 Oct 1996

---

<sup>1</sup>Visiting Astronomer, Kitt Peak National Observatory, operated by the Association of Universities for Research in Astronomy, Inc. under contract with the National Science Foundation.

## ABSTRACT

The reddening properties and the star formation history of a sample of 19 starburst galaxies are investigated using multiwavelength spectroscopy and infrared broad band photometry. New photometric data in the J, H, and K bands of the central starburst regions are supplemented with previously published spectra, covering the wavelength range 0.12-2.2  $\mu\text{m}$ . In the infrared, the reddening value derived for the stellar continuum is in agreement with that of the ionized gas, but the two values diverge at shorter wavelengths; in the UV, the mean optical depth of the dust in front of the stars is smaller, being only 60%, than the optical depth of the dust in front of the nebular gas. This difference can be better understood if the UV-bright stellar population and the ionized gas are not co-spatial. A model of foreground clumpy dust, with different covering factors for the gas and the stars, is proposed to account for the difference in reddening. A “template starburst spectrum”, derived by combining the reddening-corrected UV, optical, and infrared data of all the galaxies in the sample, is used to investigate the star formation history of the galaxies. Spectral synthesis models indicate that the observed UV emission can be attributed to a stellar population which is undergoing active star formation at a constant rate since  $\sim 2 \times 10^7$  yr, in agreement with the supernova rates derived from the [FeII] emission line in the infrared. At least two, and probably more, intermediate age populations (age  $< 2 \times 10^9$  yr) contribute to the optical and infrared emission, while populations older than  $\sim 2 \times 10^9$  yr do not contribute significantly to the template. The stellar composition of the template spectrum suggests episodic star formation over the last  $10^9$  yr, with star formation rates as large as or larger than the present rates. The synthetic stellar populations are generated according to an Initial Mass Function (IMF) with Salpeter slope ( $\alpha=2.35$ ) in the

mass range  $0.1\text{--}100\text{ M}_\odot$ , and reproduce a number of observational constraints, such as the spectral energy distribution of the template spectrum, the equivalent width of the atomic hydrogen emission lines, and the mass-to-light ratios; the data, then, do not provide indication for a high-mass-star truncated or a low-mass-star deficient IMF in starburst galaxies.

*Subject headings:* galaxies: starburst – galaxies: ISM – galaxies: photometry – ISM: dust, extinction – infrared: galaxies

## 1. Introduction

The study of the history of stellar populations plays a crucial role in understanding the evolution of galaxies, and, in this framework, starbursts may occupy a key position. In a starburst galaxy, the radiation output is dominated by the emission from a large number of recently formed, hot, massive stars. In some cases, the rate of star formation is high enough that, if it remains constant, the galaxy will be depleted of its gas content in much less than a Hubble time. The role of starbursts within the galaxy evolution scenario is still debated: are bursts of star formation the preferred channel for forming new stellar populations or are they just sporadic events in the lifetime of some galaxies? Did the first generation of stars in a primeval galaxy form from a widespread burst of star formation over a short timescale or was it created through a slow and mostly quiescent process?

In order to answer these questions, we need first to understand how starbursts evolve in local galaxies. Star formation episodes show a large variability in duration, ranging from  $10^7$ – $10^8$  yr (Rieke et al. 1985) to more than  $10^9$  yr (Hunter & Gallagher 1986). The lifespan of a star formation event is only loosely constrained by the gas depletion timescale. The mechanisms for generating inflows of gas to fuel the star forming region are not completely understood yet, although models are being investigated (e.g. Shlosman 1992). The total gas mass in a galaxy is difficult to determine, since both the atomic and molecular gas content need to be measured, but observational techniques to derive the molecular gas mass may be inadequate (e.g. Allen 1996). The gas mass available for star formation may be increased by inputs from interacting companions. Once triggered, the evolution of a starburst region depends on the details of its interaction with the galaxy environment. For instance, bursts of star formation can propagate across a galaxy, increasing the duration of the event (e.g., Beck et al. 1996). High resolution imaging reveals that bursts of star formation break down into distinct knots of OB associations, often characterized by different evolutionary

stages (Meurer et al. 1995, Conti & Vacca 1994). Finally, star formation processes can be depressed by gas outflows which may develop into superwinds and deplete a region of gas, and, therefore, of fuel (Heckman et al. 1990, De Young & Heckman 1994). It follows that feedback mechanisms from the host galaxy influence the evolution and the duration of a burst of star formation, and this is reflected into the stellar populations generated by the star-forming episode.

The universality of the stellar Initial Mass Function (IMF) in starbursts is also an open issue. A dependence of the IMF on environment may produce dramatically different results for the star formation history of the galaxy. Increasing evidence suggests, however, that the slope of the IMF in OB associations is fairly independent of the gas metallicity and close to the Salpeter value ( $\alpha=2.35$ ) in the high-mass stars regime (Massey et al. 1995, Moffat 1996, Stasinska & Leitherer 1996). The upper and lower mass limits for the IMF in starburst galaxies are still strongly debated. Stars as massive as 85–100  $M_{\odot}$  are found in the Galaxy, in the Magellanic Clouds, and in nearby resolved starbursts, suggesting upper mass limits independent of the environment (Kudritzki et al. 1991, Massey et al. 1995, Moffat 1996). Infrared studies of unresolved starburst galaxies point, however, at upper mass limits as low as 30  $M_{\odot}$  for the IMF, using either the comparison of the observed spectra with models, as in the case of the luminous infrared galaxies (Goldader et al. 1996), or the analysis of the He/H line emission ratios (Doyon, Puxley, & Joseph 1992, see however Shields 1993). Even more difficult is the determination of the low mass star limit, which cannot be directly observed, because the energy output from a starburst galaxy is dominated by the high mass stars produced in the burst. Values larger than 1  $M_{\odot}$  for the low mass limit of the IMF in starburst galaxies have been suggested on the basis of the observed mass-to-light ratios (Rieke et al. 1980, 1993, Bernlöhr 1993). These conclusions, however, depend on the adopted IMF (Rieke et al. 1993) and on the reddening correction applied to the luminosity. Revisions of the latter indicate smaller values of the low mass star limit, at least for the

famous case of M 82 (Lester et al. 1990, Satyapal et al. 1995). The analysis of a relatively large sample of galaxies shows that a low-mass-star deficient IMF is, indeed, not universal among starbursts (Devereux 1989).

Corrections for the effects of dust reddening are crucial when multiwavelength observations are used to derive intrinsic quantities for a galaxy. Dust selectively extinguishes the radiation, with blue wavelengths being more affected than red wavelengths. As an added complication, limitations in angular resolution usually produce observations of unresolved galactic regions, and the *effective* reddening of the emerging radiation is determined by the details of the dust-stars-gas geometry (Natta & Panagia 1984, Disney, Davies & Phillips 1989, Witt, Thronson & Capuano 1992, Byun, Freeman, & Kylafis 1994, Giovanelli et al. 1995, Xu & Buat 1995, Shields & Kennicutt 1995, Witt & Gordon 1996, Boisseé & Thoraval 1996). Dust obscuration in moderately reddened starburst galaxies can be well represented by a (clumpy) dust distribution foreground to the star forming region(s) (Calzetti, Kinney, & Storchi-Bergmann 1994, 1996, Kinney et al. 1994, Calzetti et al. 1995, Meurer et al. 1995). However, the reddening of the stellar continuum in these galaxies is generally lower than the reddening of the ionized gas (e.g. Fanelli, O’Connell & Thuan 1988, Calzetti et al. 1994, CKS94 hereafter, Lançon, Rocca-Volmerange & Thuan 1996, Mayya & Prabhu 1996), suggesting that the covering factor of the dust in front of the stars is lower than that in front of the gas. Generally, the effects of the dust obscuration are only partially explained by the foreground distribution. The observed UV and optical radiation accounts only for 70% of all the radiation contributing to the far infrared (IRAS) luminosity (Calzetti et al. 1995), implying that a fraction of the stars is embedded in optically thick dust clouds.

The study of the star formation histories of starburst galaxies helps to gain insight into the starburst phenomenon. New photometric data at J, H, and K are presented and discussed for a sample of 24 galaxies, and are supplemented with published UV, optical and

near infrared spectra. These data are used to investigate the reddening properties of the stellar continuum in the entire wavelength range UV-to-IR, and to derive the stellar content of starburst regions. The investigation on the dust obscuration of the stellar continuum presented here (section 4) is an extension to infrared wavelengths of the study of CKS94; the results on the reddening of the ionized gas of Calzetti et al. (1996, CKS96 hereafter) will be used. The observations are presented in sections 2 and 3. Constraints on the recent star formation history through the Type II supernova rates are derived in section 5, and the stellar content and star formation history of the galaxies are discussed in sections 6 and 7. The conclusions are presented in section 8.

## 2. The Data

### 2.1. Sample Description

The 24 galaxies listed in Table 1 include 19 starbursts, 1 LINER, and 4 Seyfert 2s, selected from the *Atlas of Ultraviolet Spectra of Star-Forming Galaxies* of Kinney et al. (1993). A galaxy had to have a well detected UV spectrum in the IUE archive in order to be included in the sample, which automatically excluded heavily reddened objects. In addition to this basic selection criterion, optical spectra obtained in apertures which closely match that of IUE had to be available (see section 2.3). For this sample, broad-band images at J, H, and K, and, for some of the galaxies, infrared (IR) spectra were obtained (see CKS96 for the IR spectroscopy).

The 24 galaxies are at low redshifts, with distances between 2.5 Mpc (NGC 1569) and 300 Mpc (Mrk 357), with median value  $\sim 60$  Mpc ( $H_0=50$  km/s/Mpc). The multiwavelength data are obtained using observational apertures which are closely matched in size, so that

the same region is sampled at all wavelengths in each galaxy. The apertures subtend physical regions of about 4.5 kpc at the typical distance of the galaxies, implying that a fairly large portion of the galaxy population is sampled. The 19 starburst galaxies span a range of morphological types, from Sab to Irregulars, usually with disturbed morphologies. The oxygen abundance ranges typically from 1/4 to twice solar (see Table 2), although abundances as low as 1/10 solar have been derived for NGC 4861 (Barth et al. 1994). A detailed description of the data used in this work is given in the following two sections.

## 2.2. The Infrared Images

The IR images were obtained with the Simultaneous Quad-color Infrared Imaging Device (SQIID) at the KPNO 1.3-m telescope during two separate runs in April 1994 and October 1994. The SQIID has four detectors which are exposed simultaneously to image a field in the J, H, K, and L' bands. Each detector has  $256 \times 256$  pixels, with a scale of 1.395"/pix, 1.366"/pix, and 1.361"/pix at J, H, and K, respectively. The overlapping area between the detectors is  $245 \times 245$  pixels (Ellis et al. 1992).

The targets were typically observed with multiple exposures of 3 minutes each, to account for the fluctuations of the sky background. Total integration times ranged from 15 minutes for the brightest galaxies to 36 minutes for the faintest galaxies. NGC 1068 was observed with multiple exposures of 5 seconds each, with total integration time of 30 seconds. Sky frames were obtained by moving the targets across the SQIID 5.5' field of view.

The data were background subtracted using DIMSUM<sup>1</sup>, which masks the objects and

---

<sup>1</sup>DIMSUM is the Deep Infrared Mosaicing Software package developed by P.



rescales the images before median filtering to create the sky frames. Flat-fielding and co-addition of the images was obtained using the SQUIID data reduction package<sup>2</sup>.

At least one blue ( $J-K < 0.1$ ) and one red ( $J-K \sim 0.9$ ) standard stars from the list of Elias et al. (1982) were observed each night for flux calibration and color corrections. The blue standards were followed through the night to provide airmass corrections. The loss in flux due to a unit change in airmass is 0.175 mag at J and K, and 0.125 mag at H.

Cross-calibration of the standard stars shows variations of about 6% in the absolute K band photometry during the April run and 7% in the same band during the September run. The uncertainties are smaller in the more sensitive J and H bands. The variations of the observed colors relative to the expected ones for the standard stars are  $\Delta(J - H) < 3\%$  and  $\Delta(H - K) < 2\%$  during the April run, and  $\Delta(J - H) < 4\%$  and  $\Delta(H - K) < 3\%$  during the September run. The variations are small, likely because of the simultaneous exposure of the J, H, and K detectors.

The observed galaxies are listed in Table 1, together with the activity type, the redshift, the K-band magnitude, the J–H color, and the H–K color, measured in an aperture of 10'' diameter centered on the starburst. All quantities have been corrected for the foreground extinction from our Galaxy (Burstein & Heiles 1982). The present sample has some overlap with the sample of Markarian galaxies analyzed by Balzano & Weedman (1981), who obtained absolute photometry at J, H, and K in an aperture comparable to the one used here. The 7 galaxies in common between the two samples are: IC 1586 (Mrk 347),

---

Eisenhardt, M. Dickinson, A. Stanford, and J. Ward, and is available upon request to prme@kromos.jpl.nasa.gov or med@stsci.edu

<sup>2</sup>The SQUIID data reduction package has been developed by M. M. Merrill and J. W. MacKenty and is available upon request to merrill@noao.edu

NGC 1614 (Mrk 617), NGC 4194 (Mrk 201), NGC 4385 (Mrk 52), NGC 6052 (Mrk297), NGC 6217, NGC 7714 (Mrk 538). Differences  $\Delta K < 0.09$  and  $\Delta J < 0.12$  are observed in the absolute photometry of the common galaxies; typical differences in the colors are less than  $\Delta(J - H) \simeq 0.07$  and  $\Delta(H - K) \simeq 0.05$ . We adopt the differences as  $1 \sigma$  uncertainties on our measurements. The differences with previous results are larger for the absolute photometry than for the colors, and can be attributed to the different filter bandpasses used in the two works, to the different calibration stars, and to atmospheric transparency variations during our observations.

### 2.3. The Ultraviolet, Optical and Infrared Spectra

The ultraviolet (UV) and optical spectra of the 19 starburst galaxies listed in Table 1 are presented in Kinney et al. (1993), McQuade, Calzetti, & Kinney (1995), and Storchi-Bergmann, Kinney, & Challis (1995). The UV (IUE) and optical spectra cover the spectral range 0.12–0.80  $\mu\text{m}$ . Quantities measured from those spectra are given in Table 2 (see also CKS94). For a subsample of 16 galaxies near-infrared (NIR) spectra were obtained (CKS96) and the data relevant to the present work are reported in Tables 3 and 4. The NIR spectra cover the wavelength range 1.236–1.340  $\mu\text{m}$  in the J band and 2.113–2.250  $\mu\text{m}$  in the K band. The optical and NIR observational apertures were closely matched to the IUE aperture ( $10'' \times 20''$ ), in order to compare similar regions at different wavelengths in each galaxy. Some of the NIR spectra are shown in Figure 1, and two examples of multiwavelength spectra are given in Figure 2.

For the 19 starburst galaxies in the sample, Table 2 reports: the intrinsic color excess from the Balmer line ratio  $\text{H}\alpha/\text{H}\beta$  (CKS94), the oxygen abundance  $\log(O/H) + 12$  (Storchi-Bergmann, Calzetti, & Kinney 1994), the  $\text{H}\alpha$  equivalent width (EW), the UV

flux density  $F(0.16)$  at  $0.16\ \mu\text{m}$ , the K-band flux density  $F(2.22)$ , and the NIR spectral index  $\beta_{im}$ . All quantities are corrected for the foreground Galactic reddening. The UV flux density is the mean value derived from the IUE spectra in the range  $0.125\text{--}0.195\ \mu\text{m}$ . The K-band flux density  $F(2.22)$  from the images is measured in a  $10''\times 20''$  window centered on the starburst region, to match the UV aperture. The IR magnitudes are converted into flux densities using the zero-points of Campins et al. (1985). The NIR spectral index  $\beta_{im}$  is derived from the flux densities at J, H, and K, assuming that the IR spectral energy distribution can be described by the power law  $F(\lambda) \propto \lambda^{\beta_{im}}$ . The J, H, and K photometric flux densities used in the fit are also extracted from a  $10''\times 20''$  window, with the same orientation of the NIR spectra (E–W), to avoid aperture mismatches with the spectroscopic data.

Tables 3 and 4 contain the data from the NIR spectroscopy: the flux and EW of the hydrogen emission lines  $\text{Pa}\beta(1.282\ \mu\text{m})$  and  $\text{Br}\gamma(2.166\ \mu\text{m})$ , the flux of the  $[\text{FeII}](1.257\ \mu\text{m})$  and the  $\text{H}_2\ v = 1 - 0\text{S}(1)$  ( $2.121\ \mu\text{m}$ ) emission lines, the intrinsic galaxy reddening from the Balmer/Brackett line ratio  $\text{H}\beta/\text{Br}\gamma$ , the K-band flux density  $F(2.18)$ , the NIR spectral index  $\beta_{sp}$ , the reddening corrected ratio  $[\text{FeII}](1.257\ \mu\text{m})/\text{H}_2(2.121\ \mu\text{m})$ , and the ratio between the two  $\text{H}_2$  transitions  $v = 1 - 0\text{S}(0)$  ( $2.223\ \mu\text{m}$ ) and  $v = 1 - 0\text{S}(1)$  ( $2.121\ \mu\text{m}$ ). For the latter, only one measurement and five upper limits could be determined. For the other galaxies, the redshift is high enough that the  $\text{H}_2$  line at  $2.223\ \mu\text{m}$  is outside the spectral range used here. The upper limits on  $\text{H}_2(2.223\ \mu\text{m})$  are calculated from the flux of the largest noise spike in the wavelength region where the line is expected to be located. The spectral index  $\beta_{sp}$  is derived via a simultaneous  $\chi^2$  fit of the J and K spectra with a power law  $F(\lambda) \propto \lambda^{\beta_{sp}}$ , after removal of the emission lines. The flux density  $F(2.18)$  is the mean value derived from the wavelength range  $2.115\text{--}2.250\ \mu\text{m}$ . The  $\text{Pa}\beta$  and  $\text{Br}\gamma$  line intensities, and the reddening values from  $\text{H}\beta/\text{Br}\gamma$  appeared in CKS96 for 13 of the 16 galaxies in Table 3; those values are listed here for convenience, since they will be frequently used in

the following sections. The comparison of the  $\text{Pa}\beta$  and  $\text{Br}\gamma$  line fluxes measured here with values published in the literature is discussed in CKS96. For the  $[\text{FeII}]$  and  $\text{H}_2(2.121\ \mu\text{m})$  emission lines, only three galaxies are in common between this and other samples: the  $\text{H}_2$  line fluxes of NGC1614 and NGC6090 are given in Goldader et al. (1995); the  $[\text{FeII}]$  line flux of NGC1614 in Puxley et al. (1994); and the  $\text{H}_2$  and  $[\text{FeII}]$  line fluxes of NGC7714 in Moorwood & Oliva (1988). The aperture sizes used by these authors are 4 to 5 times smaller than those used here. Their line measurements give fluxes which are 2 to 5 times smaller than ours, pointing at the extended nature of the  $[\text{FeII}]$  and  $\text{H}_2$  emission in these galaxies.

#### 2.4. The Infrared Images-Spectra Comparison

The K-band flux densities from the images are systematically 10–15% lower than the analogous flux densities from the spectra. The spectra cover only  $\sim 0.1\ \mu\text{m}$  in wavelength range, about 1/6 of the typical K bandpass used for the images. The transformation from one to the other, therefore, carries uncertainties due to the unknown behaviour of the galaxies energy distribution in the wavelength range not covered by the spectra. This, coupled with the fact that variations of the atmospheric transparency were larger during the imaging observations than during the spectroscopic observations, may ultimately account for the mismatch.

The NIR spectral index derived from the spectra,  $\beta_{sp}$  must have the same value of the index from the images,  $\beta_{im}$ , if the relative calibration of different wavebands has been done correctly. Figure 3 shows that this is the case for 14 of the 16 galaxies in Table 4. The two exceptions are IC 1586 and Mrk 542, whose spectra were obtained in poor weather conditions. An uncertainty of less than 30% in the calibration of the J spectra relative to the

K spectra produces a variation  $\delta\beta_{sp} = 0.5$ . In the next sections, the NIR colors associated with the two galaxies will be those from the imaging, since the J, H, and K images were obtained simultaneously, and are thus almost independent of the sky conditions.

### 3. Infrared Colors

The starburst, LINER, and Sy2 galaxies in our sample occupy the typical loci expected for these classes of galaxies in the (J–H)–(H–K) diagram (see Figure 4; e.g. Carico et al. 1986). Only NGC 4861 and NGC 1068 deviate from the general trend. The J–H color of NGC 4861 is bluer than the other starbursts and is due to the Pa $\beta$  emission line’s contribution to the J-band magnitude (Table 3). The Pa $\beta$  EW of 200 Å corresponds to about 9% of the J-band flux; after the line removal, the galaxy’s IR color becomes J–H=0.47, closer to the expected value for the stellar continua of bursts of star formation.

The Seyfert 2 and LINER galaxies in our sample, except NGC 1068, are indistinguishable from the starbursts in the (J–H)–(H–K) plane (e.g. Carico et al. 1990). Although the intrinsic colors for Seyfert nuclei are expected to be J–H $\sim$ 0.95 and H–K $\sim$ 1.05 (Glass 1981), the 10'' aperture subtends galaxy regions of  $\sim$ 2–4 kpc in size, and the contribution to the IR flux from the host galaxy and/or the circumnuclear burst of star formation is significant (e.g. Heckman et al. 1995a). The NIR colors of NGC 1068 are much redder than the other 3 Sy 2’s, as already known from previous investigations (e.g. Scoville et al. 1988). This galaxy is closer to our Galaxy than the other Sy2’s by a factor 2 to 4. The physical region sampled by the 10'' aperture has a linear scale of about 1 kpc, smaller than the inner radius of the circumnuclear starburst ring (about 1.5 kpc, Heckman et al. 1995a). The IR colors of NGC 1068 become bluer for increasing aperture size (Figure 4, cf. Scoville et al. 1988), as expected if the contribution from the stars of the host galaxy increases. The

colors of an annulus with inner and outer radii of  $15''$  and  $30''$ , respectively, embracing the circumnuclear burst of star formation (Heckman et al. 1995a), are consistent with those of the starburst galaxies. The H–K color of the nucleus of NGC 1068 (in the  $5''$  aperture) is redder than the expected value for Seyferts. If the intrinsic color of the non-thermal nuclear source is H–K=1.05, and if hot dust emission in the K-band is the cause for the red H–K color (Carico et al. 1990), then the hot dust provides about 50% of the flux at  $2.2\ \mu\text{m}$ .

## 4. Reddening

### 4.1. The Reddening of the Stellar Continuum

The properties of the starburst galaxies in the sample cannot be properly discussed without investigating the impact of the dust obscuration on the measured fluxes. The analysis of the dust reddening in external galaxies is usually complicated by the potentially complex geometries which characterize the distribution of stars, ionized gas, and dust. Even in the presence of fairly large amounts of dust, mixed distributions of the various components can mimick a grey obscuration, and give the (incorrect) impression that the reddening in the galaxy is negligible (e.g., Witt, Thronson, & Capuano 1992). In addition, the obscuration suffered by the stellar continuum may be different from the obscuration of the ionized gas, since stars and gas may occupy different locations within the galaxy, and the dust may have different covering factors for stars and gas. Various authors (e.g., Fanelli et al. 1988, CKS94, Lançon et al. 1996) have reported that the emission from stars is typically less obscured than the emission from the ionized gas. However, CKS94 showed that the reddening of the UV continuum emission (i.e., massive stars) correlates with the reddening of the gas. In this and the next section we use the infrared observations presented

in section 2 to pin down the effects of obscuration on the stellar continuum of the sample galaxies, and to derive a description for the geometrical distribution of the dust. For the reddening of the nebular gas, the results by CKS96 are adopted.

From the analysis of the hydrogen emission line intensities at optical and infrared wavelengths, CKS96 conclude that the geometry of the dust obscuring the ionized gas can be described by a foreground clumpy distribution, and the reddening is compatible with a Galactic-like extinction curve. Although the solution for the geometry is not unique (see Puxley & Brand for the case of NGC1614), it represents a simple description which accounts for the observed reddening values of the gas in the optical+IR wavelength range (up to Br $\gamma$ ). The same study excludes pure internal dust as a viable geometrical description.

The dust obscuration becomes progressively less important towards IR wavelengths; the Galactic extinction is about 10 times smaller at 2.2  $\mu\text{m}$  than at 0.55  $\mu\text{m}$ . The effects of dust reddening on the stellar continuum can then be investigated using multiwavelength observations. If the shape of the galaxy continuum spectrum is determined by the overall effect of the dust, rather than by the details of the intrinsic stellar population, the variations of the continuum strength can be interpreted as due to dust reddening. The ratio of the flux density at  $\lambda_X$  to the K-band flux density,  $\log F(\lambda_X)/F(K)$ , can be studied as a function of the color excess  $E(B-V)_{H_a/H_b}$ , derived from a pair of hydrogen emission lines  $H_a$  and  $H_b$ , to gain insight in the geometrical distribution of the dust associated with the starburst region. The standard definition of the color excess (see, e.g. CKS96):

$$E(B - V)_{H_a/H_b} = \frac{\log(R_{obs}/R_{int})}{0.4[k(\lambda_a) - k(\lambda_b)]}, \quad (1)$$

will be used in the following derivation.  $R_{int}$  and  $R_{obs}$  are the intrinsic and observed hydrogen line ratios, respectively, and  $k(\lambda)$  is the extinction curve, measured at the wavelength of the emission line. The curve  $k(\lambda)$  is defined as the total-to-selective extinction of the gas,  $A(\lambda)/E(B-V)$ , where  $A(\lambda)$  is the attenuation in magnitudes. Both the extinction

curves of the Galactic diffuse ISM and of the 30 Doradus region in the Large Magellanic Cloud are used in the analysis. At optical wavelengths, the Galactic curve is parametrized according to Seaton (1979) and the 30 Dor curve according to Fitzpatrick (1986). In the IR, the parametrization of Landini et al. (1984) is adopted for both the extinction curves. For the color excess, both the standard Balmer ratio  $H\alpha/H\beta$  and the ratio  $H\beta/Br\gamma$  are used. The latter has the advantage of a long wavelength baseline, which reduces the effects of measurement uncertainties (CKS96). The adopted values for the differential extinction suffered by the hydrogen lines are:  $k(H\beta)-k(H\alpha)=1.17$  and  $k(H\beta)-k(Br\gamma)=3.35$ .

The  $F(\lambda_X)$  flux densities selected for the analysis are centered at  $\lambda_X=0.16, 0.26, 0.44, 0.55, 0.70, 1.25$ , and  $1.65 \mu\text{m}$ . The UV flux densities,  $F(0.16)$  and  $F(0.26)$ , are the mean values in  $0.06 \mu\text{m}$  wide emission bands; the optical flux densities are obtained from  $0.09 \mu\text{m}$  or  $0.1 \mu\text{m}$  wide bands, after removal of the emission lines. The  $F(1.25)$  and  $F(1.65)$  flux densities are from the J and H band measurements, respectively (Tables 2 and 4). The K-band flux densities are used as reference point for the continuum emission at shorter wavelengths. Examples of stellar continuum ratios as a function of the color excess measured from the hydrogen recombination lines are given in Figure 5.

A (mostly) linear correlation can be discerned at all wavelengths, and the linear fits to the flux density ratios are expressed as:

$$\log[F(\lambda_X)/F(K)] = s E(B - V)_{H_a/H_b} + \log[F_o(\lambda_X)/F_o(K)], \quad (2)$$

where  $F_o(\lambda_X)/F_o(K)$  is the intrinsic flux density ratio at the specified waveband  $\lambda_X$ . For  $H_a/H_b=H\alpha/H\beta$ ,  $F(K)=F(2.2)$ , whereas for  $H_a/H_b=H\beta/Br\gamma$ ,  $F(K)=F(2.18)$ . The linear correlation between the stellar continuum flux ratios and the color excess of the ionized gas indicates that the reddening of the gas is proportional that of the stars (CKS94). Although complex geometrical distributions of dust, gas, and stars still are not excluded, an ‘effective’



obscuration curve for the stellar continuum can be defined as:

$$k'(\lambda_X) - k'(K) = -s/0.4, \quad (3)$$

where

$$k'(\lambda) = \frac{A'_{star}(\lambda)}{E(B - V)_{gas}}, \quad (4)$$

with  $A'_{star}(\lambda)$  the effective attenuation of the stellar continuum. The selective obscuration of the stellar continuum,  $k'(\lambda_X) - k'(K)$ , is then normalized to the color excess of the gas.

The list of values for  $k'$  at different wavelengths is reported in Table 5, together with the intrinsic flux density ratios, the number of points used in each fit, and the reduced  $\chi^2$ . The continuum flux density ratios are fitted using  $E(B-V)_{H\alpha/H\beta}$  as independent variable for the IR images, and  $E(B-V)_{H\beta/Br\gamma}$  for the spectra. The lower number of data available from spectroscopy is usually compensated by tighter correlations, resulting in smaller values of the reduced  $\chi^2$  and in comparable  $1\sigma$  uncertainties in the two data sets. The galaxies NGC 4861 and IC 214 do not follow the same trend as the others at UV and optical wavelengths, respectively, and are removed from the fits. NGC 4861 is in any respect a peculiar galaxy in our sample; the large EWs of its emission lines suggest an overall stellar population which is much younger than the average of the other galaxies in the sample. Both the continuum and the line emission from NGC 4861 are dominated by the Bright Knot, a giant HII region with an upper limit on the age of  $\sim 4.5$  Myr (Barth et al. 1994, see also section 7). For IC 214, the deviation can be attributed to the absolute calibration of the optical spectrum, which appears underestimated. There are only 8 galaxies in our sample for which  $F(0.26)$  is available, therefore the data point  $k'(0.26) - k'(K)$  has the largest uncertainty. The values of  $k'(\lambda)$  are shown in Figure 6, together with the curve obtained by CKS94 at UV and optical wavelengths. CKS94 could not derive the absolute value for the obscuration curve, and their curve is here arbitrarily placed at  $k'(0.55) - k'(2.2) = 2$ , which is approximately the halfway point between the two

sets of values obtained from  $E(B-V)_{H\alpha/H\beta}$  and from  $E(B-V)_{H\beta/Br\gamma}$  (see Table 5). The  $k'(\lambda)$  values derived from the  $E(B-V)_{H\beta/Br\gamma}$  correlations are systematically higher than the values derived from the  $E(B-V)_{H\alpha/H\beta}$  correlations. The two sets of data do not appear to be drawn from two different populations; however, the  $H\beta/Br\gamma$  set underpopulates the region of low color excess values. The differences in  $k'(\lambda)-k'(2.2)$  can therefore be attributed to the statistical uncertainty associated with the small number of points on which the linear fits are performed. Hence, we adopt the dispersion of the two datasets as the actual uncertainty in our measurements.

For the Galactic diffuse interstellar medium, the total-to-selective extinction at optical wavelengths is  $k(0.55)=3.1$ , and the selective extinction is  $k(0.55)-k(2.2)=2.8$ . The mean value of  $k'(0.55)-k'(2.2)$  is  $\sim 2$  for the obscuration curve of Figure 6, smaller than the Galactic value. The present data are not suited for deriving the total-to-selective obscuration at optical wavelengths  $k'(0.55)$ , because we are lacking the reference point at zero obscuration (e.g. radio data). However, since the total-to-selective obscuration at K,  $k'(2.2)$ , is expected to be small, and probably not larger than the corresponding Galactic value  $k(2.2)=0.3$ ,  $k'(0.55)$  should be only a few tenths larger than  $k'(0.55)-k'(2.2)$ . It follows that the total-to-selective obscuration in the starburst galaxies is smaller than the total-to-selective Galactic extinction. This method normalizes the obscuration curve to the color excess of the nebular gas [equation (4)]; as will be seen in the next section, the shallow trend of  $k'(\lambda)$ , especially at UV wavelengths, can be interpreted as a difference in the covering factors of the dust in front of the stars and of the gas.

Emission from hot dust may in principle originate around HII regions, where the high UV energy density may heat a fraction of the available dust to high temperatures ( $T \geq 500$  K, e.g. Panagia 1978), and contribute to the K-band flux. A contribution to the K-band proportional to the amount of reddening from the hot dust would bias the slope

$s$  of Equation 2 by increasing its absolute value, and making it more negative. However, the K-band flux of the “dusty” starburst galaxy M 82 receives less than 15% contribution from hot dust (Satyapal et al. 1995). In addition, bluer wavelengths are progressively less affected by hot dust emission than the K band, and our results on  $k'(\lambda)$  do not change if the J band instead of the K band is chosen as reference point.

Two basic hypotheses are used in deriving  $k'(\lambda)$ : 1) the stellar continuum ratios  $F(\lambda_X)/F(K)$  are mostly determined by dust reddening and the variations in the composition of the stellar population in each galaxy are a secondary effect; 2) the ageing of the burst population is also a secondary effect. To test these hypotheses, the observed continuum ratios  $F(0.55)/F(0.16)$  and  $F(2.2)/F(0.55)$  of the 19 galaxies are compared with predictions from models of stellar populations in Figure 7. The two extreme cases of a single, ageing burst population and of a continuous star formation population, in the age range  $1 \times 10^7 - 1.5 \times 10^{10}$  yr, are considered (Bruzual & Charlot 1996, Leitherer & Heckman 1995, LH95 hereafter, see also section 6). In neither case, the predicted colors are able to reproduce the observed ones. The reddening lines are also shown, using the Galactic and LMC extinction curves and the curve of Figure 6. The trend of the data points is compatible with being mostly due to dust obscuration, and the scatter around the reddening line can be attributed to variations in the intrinsic populations from galaxy to galaxy. Some scatter is indeed expected due to the large galaxy region subtended by the observational apertures. The separate position occupied by NGC 4861 in the diagram is a consequence of the younger stellar population which characterize this galaxy relative to the others (see section 7). The location of IC 214 is explained by the inaccurate calibration at optical wavelengths.

Further evidence that the reddening and not the ageing of the burst population is the main responsible for the observed trends comes from the study reported in CKS94.

In starburst galaxies, the UV spectral index is weakly dependent on age; the number of ionizing photons decreases significantly (and the nebular lines becomes undetectable) before the intrinsic value of the UV spectral index changes appreciably (LH95). Therefore, the correlation of the UV spectral index with the color excess  $E(B-V)$  of the gas, found by CKS94, is an effect of dust reddening; the ultraviolet stellar continuum becomes redder as the reddening of the gas increases.

## 4.2. A Model for the Reddening

The distribution of stars, gas, and dust in galaxies is complex enough that in general it cannot be fully accounted for by simple models. However, models provide pictorial guidelines on the true distribution, and, in some cases, can satisfactorily describe the observables, such as the reddening of the emerging radiation.

The foreground clumpy dust model, which is able to describe the reddening of the nebular gas (CKS96), will be employed to pin down any difference between the obscuration of the stellar continuum and the obscuration of the gas, from the UV to the K band. In the model, the dust clumps are assumed to be all equal and to be Poissonian distributed along the line of sight, with average number  $\mathcal{N}$  (Natta & Panagia 1984, CKS94). The clumpy distribution is also assumed to be foreground to the ionized gas, and, therefore, to the starburst region; however, it is not required that it is foreground to the entire galaxy. It should be remembered that the goal of the model is to provide some insight on the systematic behavior of the reddening suffered by the stars, but may not necessarily yield the *exact* geometrical distribution of the dust in the galaxy.

The general expression for the color excess of the radiation crossing a foreground

distribution of clumps is given by (CKS94):

$$E(B - V)_{H_a/H_b} = 1.086 \mathcal{N}^g \frac{e^{-\tau_c(H_b)} - e^{-\tau_c(H_a)}}{k(H_a) - k(H_b)}, \quad (5)$$

where  $H_a$  and  $H_b$  are defined as in Equation (1),  $\mathcal{N}^g$  is the average number of clumps crossed by the nebular radiation,  $\tau_c(\lambda)$  is the optical depth of a clump at wavelength  $\lambda$ , which satisfies the relation  $\tau_c(\lambda_a)/\tau_c(\lambda_b) = k(\lambda_a)/k(\lambda_b)$ , and  $k(\lambda)$  is the extinction curve (e.g., Galactic or LMC). Two cases are shown in Figure 8, overplotted to the data of CKS96, and correspond to two configurations of the relative source-dust location. In the first case (dashed line in Figure 8), the dust layer is close to the radiation source, so light from regions outside the observational aperture is scattered into the line of sight, and adds a positive contribution to the observed radiation (scattering model, this is also the case shown in Figure 1 of CKS96). In the second case (continuous line), such “extra” contribution is not present, because the clumpy dust layer is distant from the radiation source, or because the observational aperture is large enough to encompass most of the scattering regions (non-scattering model). The non-scattering model is in better agreement with the observed color excess than the scattering model, and is used to investigate the behavior of the stellar continuum. The agreement with the data of the non-scattering case is not surprising, since the observational aperture encompasses a major fraction of the galaxy at the typical distance of 60 Mpc.

Since the reddening of the stellar continuum correlates with the reddening of the nebular gas, the same model can be employed to describe the obscuration of gas and stars. However, the possibility that the covering factor of the dust changes from gas to stars should be included. For a foreground distribution of clumps, the selective obscuration of the stellar continuum relative to the emission lines,  $k'(\lambda) - k'(2.2)$ , is then given by (CKS94):

$$k'(\lambda) - k'(2.2) = f \frac{[e^{-\tau_c(2.2)} - e^{-\tau_c(\lambda)}]}{[e^{-\tau_c(H_b)} - e^{-\tau_c(H_a)}]} [k(H_a) - k(H_b)], \quad (6)$$

where  $f = \mathcal{N}^s/\mathcal{N}^g$  is the ratio of the average number of clumps in front of the stars to the number in front of the ionized gas (i.e., the ratio between covering factors). The shape of the curve in Equation (6) depends on the optical depth of the clumps, and on the two emission lines  $H_a$  and  $H_b$  selected for the normalization; however, for our range of optical depths,  $\tau_c(0.55) < 3.7/\mathcal{N}^g$  or, if  $\mathcal{N}^g > 10$ ,  $E(B-V)_{H\beta/Br\gamma} < 1$ , such dependences are not important.

The effect of the parameter  $f$  on the selective obscuration described by Equation (6) is shown in Figure 9. If both the ionized gas and the stars cross the same dust layer,  $f = 1$ ; the case shown in the figure (curves 1G and 1L) corresponds to  $\mathcal{N}^g=10$  and  $E(B-V)_{H\beta/Br\gamma}=1.0$ , which implies  $\tau_c(0.55) = 0.37$ . The predicted optical and UV rise is clearly steeper than the observed one, and the disagreement is not lessened if the model parameters are changed: the dependence on  $\tau_c$  is weak for our range of values, and there is no explicit dependence of the curve on the average amount of clumps  $\mathcal{N}$ . However, changing the value of  $f$  changes the normalization of the obscuration curve. A qualitative agreement between data and models is observed in Figure 9, for both the Galactic and the LMC extinction curves, if  $f = 0.6$  is adopted (curves 2G, 2L, 3G, and 3L). From a quantitative point of view, small disagreements still exist between data and models: the Galactic curve has in general too strong a  $0.22 \mu\text{m}$  feature, and the LMC curve is too steep in the far-UV, relative to the CKS94 curve. These deviations are accentuated for small values of  $\tau_c(0.55)$ , although in such regime the reddening effect of the dust on the emerging radiation is small, and the details of the selective obscuration are lost in the measurement uncertainties.

Physically,  $\mathcal{N}^s/\mathcal{N}^g = 0.6$  means that the stellar continuum radiation crosses only 60% of the clumps crossed by the nebular radiation before emerging from the galaxy. The covering factor of the dust in front of the gas is then almost twice as much as the covering factor of the dust in front of the stars. The dust distribution is not only clumpy, but is

also unevenly distributed in front of stars and gas, and the ionized gas is, on average, more closely associated with the dust than the stars are (cf. CKS94; see, however, Keel 1993). These results on the reddening of the stellar continuum in starbursts will be applied in sections 6 and 7 to derive the intrinsic shape of the spectra.

## 5. The Iron Emission and the Supernova Rate

A first constraint on the star formation histories of our galaxies can be obtained from the comparison of the present supernova rate, which is a measure of the past star formation activity, with the present rate of production of ionizing photons, which is a measure of the current star formation activity (Kennicutt 1983). The infrared [FeII] emission line can be used to derive the present supernova rate (Moorwood & Oliva 1988, Greenhouse et al. 1991). The [FeII] line at  $1.257\ \mu\text{m}$  and the molecular hydrogen emission  $\text{H}_2\ v=1-0\ S(1)$  at  $2.121\ \mu\text{m}$  were detected in 14 of the galaxies listed in Table 3.

The [FeII] emission is believed to be linked to supernova activity (Moorwood & Oliva 1988, Greenhouse et al. 1991, Forbes & Ward 1993, Mouri, Kawara, & Taniguchi 1993, van der Werf et al. 1993, Armus et al. 1995). Iron is a refractory element heavily depleted on dust in the diffuse ISM (e.g. De Boer, Jura & Shull 1987). Fast shocks propagating in the diffuse ISM ( $v \geq 100\ \text{km/s}$ ), as those produced by supernova explosions or by superwinds, can destroy dust grains through sputtering processes or grain-grain collisions, and replenish the ISM with gas-phase iron (e.g. Draine 1990). The gaseous iron is then collisionally excited in the cooling post-shock gas, and produces the observed infrared emission (Shull & Draine 1987). Supernova remnants show enhanced [FeII]/H ratios, up to about a factor 1000 more than HII regions (e.g., Graham, Wright & Longmore 1987, Oliva, Moorwood & Danziger 1989). In galaxies, the [FeII] emission appears to be positionally coincident

with the radio emission from SNRs (Greenhouse et al. 1991, Forbes et al. 1993), and with regions of star formation (van der Werf et al. 1993, Armus et al. 1995).

Unlike the case of [FeII], more than one mechanism can produce the infrared emission from molecular hydrogen, and both nonthermal processes, like fluorescent excitation of  $\text{H}_2$  (Black & van Dishoeck 1987), and thermal processes are involved. In the thermal processes, collisionally excited  $\text{H}_2$  is present on the surface of molecular clouds heated by shocks, or UV and transient soft X-ray radiation (Draine, Roberge, & Dalgarno 1983, Hollenbach & McKee 1989, Sternberg & Dalgarno 1989, Draine & Woods 1990). Such processes appear to be the dominant mechanism for producing the  $\text{H}_2$   $v=1-0S(1)$  emission in galaxies (Moorwood & Oliva 1990, Elston & Maloney 1990, Israel & Koornneef 1991, Kawara & Taniguchi 1993, Forbes & Ward 1993, van der Werf et al. 1993). In thermal processes, the line ratio  $1-0S(0)(2.22\ \mu\text{m})/1-0S(1)(2.12\ \mu\text{m})$  is predicted to be  $<0.4$  (Mouri 1994); the upper limits on the line ratios of our galaxies (Table 4) are consistent with this requirement. Shocks from supernova explosions, superwinds, and collisions of interstellar media in mergers (Rieke et al. 1985, van der Werf 1993) compete with the UV radiation from OB associations to excite  $\text{H}_2$  in galaxies (e.g, Puxley et al. 1990, Israel & Koornneef 1991). Slow shocks ( $v < 50\ \text{km/s}$ ) are required to excite  $\text{H}_2$  (Draine et al. 1983), because fast shocks dissociate it. However  $\text{H}_2$  can form again in the cooling post-shock gas of a fast shock (Hollenbach & McKee 1989); in addition, shocks can be slowed down in the transition from the low density diffuse ISM into the high density molecular cloud (van der Werf et al. 1993, and references therein).

The distribution of the line intensities of [FeII] and  $\text{H}_2$  relative to the hydrogen recombination lines is shown in Figure 10. Most of the starbursts crowd around the values  $[\text{FeII}]/\text{Pa}\beta \sim 0.3$  and  $\text{H}_2/\text{Br}\gamma \sim 0.5$ , and have  $[\text{FeII}]/\text{H}_2$  ratios in the range 2–6 (cf. column 6 of Table 4), in agreement with previous results (Moorwood & Oliva 1988, Greenhouse et al.



1991, Goldader et al. 1995). The ratio  $[\text{FeII}](1.257 \mu\text{m})/\text{Pa}\beta$  can be related to the more widely used ratio  $[\text{FeII}](1.644 \mu\text{m})/\text{Br}\gamma$  by using  $[\text{FeII}](1.257 \mu\text{m})/[\text{FeII}](1.644 \mu\text{m})=1.36$  from the atomic data of Nussbaumer & Storey (1988), and  $\text{Pa}\beta/\text{Br}\gamma=5.72$  from case B recombination with electron temperature  $T_e=7500$  K and density  $n_e=100 \text{ cm}^{-3}$  (Osterbrock 1989). The  $[\text{FeII}]/\text{H}_2$  values are corrected for intrinsic reddening, using the color excess from the  $\text{Pa}\beta/\text{Br}\gamma$  ratio and adopting the Galactic extinction curve (CKS96), with the assumption that  $[\text{FeII}]$ ,  $\text{H}_2$ , and  $\text{H}$  are affected by the same obscuration. The LINER NGC 6764 has ratios  $[\text{FeII}]/\text{Pa}\beta=1.06$  and  $\text{H}_2/\text{Br}\gamma=2.62$ , larger than the typical values of starburst galaxies, but compatible with galaxies with active nuclei and with mergers (see, e.g., the compilation in Greenhouse et al. 1991, and van der Werf et al. 1993). In a flux-flux diagram, the correlation of  $\text{H}_2$  with the  $\text{H}$  recombination lines is less tight than the correlation of  $[\text{FeII}]$  with the  $\text{H}$  lines (see Figures 11 and 12). This supports the idea that the excitation mechanisms of  $\text{H}_2$  are not directly related to the excitation mechanisms of hydrogen or  $[\text{FeII}]$ , but are likely a mixture of more than one process (cf. Forbes & Ward 1993, van der Werf et al. 1993, Moorwood & Oliva 1994, Mouri 1994).

The  $[\text{FeII}]$  emission from a galaxy may be thought of as a measure of the “current” supernova rate (Greenhouse et al. 1991), since the  $[\text{FeII}]$ -emitting lifetime of a single supernova remnant is believed to be rather short,  $\sim 10^4$  yr (Oliva et al. 1989). The nebular  $\text{H}$  emission can be used to derive a “predicted” Type II supernova rate, because it gives a measure of the number of massive stars which are presently ionizing the gas. The total number of Type II supernovae (SNII) produced by an instantaneous burst of star formation is at most a factor 2 lower than the total number of Type Ia supernovae (SNIa), but is spread over timescale about 30 times shorter (Greggio 1996). It follows that in a steady star formation regime, the SNII rate is about one order of magnitude larger than the SNIa rate, as observed for late type spirals (van den Bergh & Tamman 1991). In this case, the  $[\text{FeII}]$  emission is produced mainly by shocks from SNII (and from SNIb, if these arise from

massive stars, see Ratnatunga & van den Bergh 1989), and is a measure of star formation activity in the recent past.

The tight correlation between [FeII] and the H recombination lines for the starburst galaxies in this sample (with the exception of NGC 4861 and NGC 1569, see below) suggests that the current supernova rate yields numbers which are proportional to the predicted supernova rate. The galaxies are characterized by similar values of the oxygen abundance (CKS94), therefore metallicity effects should not be important here. In an instantaneous burst of star formation, the number of ionizing photons decreases by 2 orders of magnitude after 7–8 Myr, while the first Type II supernova appears after 3–5 Myr (LH95). It is unlikely that all the galaxies in this sample are in the narrow evolutionary window between 4 and 8 Myr, and we favor continuous star formation to explain the tight correlation of Figure 12. This merely says that the spatial region sampled by our spectra is large enough, being typically  $\sim 4.5$  kpc in diameter, to encompass more than one star-forming knot (cf. Meurer et al. 1995), and the star formation histories of individual knots are averaged into a “global” star formation event.

Continuous star formation is also supported by the small dispersion around the mean shown by the reddening-corrected UV/K stellar continuum ratio (see Table 5 and Figure 5a). The largest observed dispersion is about  $\pm 0.2$  dex, while the UV/K ratio of a stellar population generated by an instantaneous burst of star formation changes by 1.7 dex over  $10^7$  yr, for a Salpeter IMF with upper mass limit  $100 M_{\odot}$  (using the LH95 models with solar metallicity). The variation in the UV/K ratio is smaller, about 0.7 dex, for a timescale of  $5 \times 10^6$  yr, that is, before the supergiant stars begin to contribute to the K-band flux. If the starburst events in our galaxies were generated by instantaneous bursts, they should have fine-tuned ages, in order to be all observed within the narrow range of a few Myr.

The correlation between [FeII] and Pa $\beta$  is fit by:

$$[FeII](1.257 \mu) = 0.34 Pa\beta. \quad (7)$$

Assuming a mean [FeII] luminosity of a few times  $10^3 L_{\odot, bol}$  for a supernova remnant (van der Werf et al. 1993, Oliva et al. 1989), the current supernova rate of the galaxy can be written:

$$snr([FeII]) = \frac{L_{[FeII]}/L_{\odot, bol}}{6.6 \times 10^7 (E_{\odot}/10^{51} ergs)}, \quad (8)$$

where the formula used by van der Werf et al. (1993) has been adapted to the iron emission at  $1.257 \mu m$ , with the [FeII] luminosity expressed in units of the bolometric solar luminosity, and  $E_{\odot}$  is the mean energy released in the supernova explosion (see, also, Colina 1993). The hydrogen recombination lines can be used to derive a star formation rate (SFR) and to predict a supernova rate. From LH95, with a Salpeter IMF, the SFR derived from the Br $\gamma$  line is:

$$SFR_{100} = 6.17 \times 10^{-40} L(Br\gamma), \quad (9a)$$

for a stellar mass range 0.1–100  $M_{\odot}$ , and:

$$SFR_{30} = 2.67 \times 10^{-39} L(Br\gamma), \quad (9b)$$

for a stellar mass range 0.1–30  $M_{\odot}$ . The predicted supernova rate for a minimum mass of 8  $M_{\odot}$  for a star to explode is (Elson, Fall & Freeman 1989):

$$snr \simeq 0.006 \Gamma SFR. \quad (10)$$

$\Gamma$  is the ratio of the SNII+SN Ia rate to the SNII rate (and possibly SNII+SN Ib rate, if the SN Ib have massive progenitors); this ratio is close to 1 for our purposes. Table 6 lists for each galaxy the [FeII] ( $1.257 \mu m$ ) luminosity, the SFR<sub>100</sub>, the SFR<sub>30</sub>, and the three supernova rates derived from the iron luminosity, and from the two star formation rates, respectively. The predicted supernova rates from the SFRs bracket the current supernova

rate derived from the [FeII] luminosity, consistent with the continuous star formation scenario. The agreement between the various snr estimators is reasonable if uncertainties in the energy released by supernovae, in the intrinsic [FeII] luminosity of each supernova, in the SNII/SNIa ratio, and in the IMF used to derive the SFR are accounted for.

The [FeII]/H ratios of NGC1569 and NGC4861 are one order of magnitude or more below the average (see Figures 10 and 12). The H<sub>2</sub>/H ratios are also low, although, given the large spread in the values of the other galaxies, they are not as remarkable as the iron (see Figure 11). NGC 4861 and NGC 1569 are the two nearest galaxies in the sample, and are two metal-poor dwarfs, with oxygen abundance  $12 + \log(O/H) \simeq 8.3$  (Storchi-Bergmann et al. 1994) or lower (Barth et al. 1994). Metallicity effects can explain the low [FeII]/H ratios only if the [Fe/O] abundance ratio is altered (see Gilmore & Wyse 1988), since the two galaxies have on average 1/3 of the oxygen abundance of the other galaxies, and more than one order of magnitude difference in the average [FeII]/H. The NIR recombination lines of NGC 4861 are dominated by the emission from the Bright Knot, which is a high ionization region with an estimated age of  $\sim 4.5$  Myr (Barth et al. 1994) and electron temperature and density  $T_e \sim 14,000$  K and  $n_e \sim 100 \text{ cm}^{-3}$  (Dinerstein & Shields 1986). The photoionization equilibrium thus favors ionization states of iron higher than [FeII] (Greenhouse et al. 1991), and may also account for the lower than average H<sub>2</sub> emission (Puxley et al. 1990). In addition, the first supernova explodes around 3-5 Myr, depending on the IMF upper mass limit (Leitherer, Robert & Drissen 1992). Few supernovae may have been produced by the current star formation episode, and the mechanical energy released into the ISM may be still insufficient to free a significant amount of iron into the gas-phase. Other HII regions which surround the Bright Knot are not as bright (Barth et al. 1994), and do not contribute significantly to the integrated properties. At the distance of NGC 1569 (about 2.5 Mpc, O’Connell, Gallagher, & Hunter 1994), the NIR spectroscopic aperture subtends a region of  $240 \times 85 \text{ pc}^2$ . A close inspection of the NIR spectra of NGC 1569 reveals contributions

from two knots, which are identified with the postburst super-star cluster A (Hodge 1974, O’Connell et al. 1994) and with the bright HII region “2” (Waller 1991). The HII region “2” is responsible for  $\simeq 85\%$  of the line emission in the NIR spectra, while Region A provides  $\simeq 65\%$  of the continuum. The HII region is presently among the most active sites of star formation in the galaxy, with an upper limit on the age  $\sim 5$  Myr (Waller 1991). Region A has been the site of a powerful star formation episode about 15 Myr ago (O’Connell et al. 1994), and, together with Region B, is now driving a gas outflow (Heckman et al. 1995b). For the HII region, considerations similar to NGC 4861 apply. For Region A, the superwind generated by the starburst may have already ejected from the small region subtended by our aperture significant amounts of interstellar gas and dust (Marlowe et al. 1995, Heckman et al. 1995b).

## 6. Star Formation History

### 6.1. The Template Starburst Spectrum

The reddening correlations of section 4.1 provide a method to correct the spectral energy distribution of the starburst galaxies for the effects of dust obscuration. The reddening-corrected flux densities can then be used to study the star formation histories of the galaxies in the sample.

Because of the large observational aperture employed, the observed spectra must receive a sizeable contribution from stellar populations other than the one produced by the current star formation event. Indeed, the values of the EWs of the hydrogen emission lines are smaller than expected from a single young stellar population. The average values are 100 Å, 18 Å, and 14 Å, for  $H\alpha$ ,  $Pa\beta$ , and  $Br\gamma$ , respectively, with dispersions around the

means of about 60%. The H $\alpha$  EWs are corrected for the differential reddening between lines and continuum, using the multiplicative factor  $10^{0.4E(B-V)[k(\lambda)-k'(\lambda)]}$ ; the IR lines are only mildly affected by this problem (see Table 5). If the star formation episode has been sustained at a constant rate over a few million years, as suggested by the comparison between the current and the predicted supernova rate in the previous section, then the expected values for the EWs of the hydrogen emission lines are much larger than measured, with  $\text{EW}(\text{H}\alpha) > 500 \text{ \AA}$ ,  $\text{EW}(\text{Pa}\beta) > 100 \text{ \AA}$ , and  $\text{EW}(\text{Br}\gamma) > 60 \text{ \AA}$  (from LH95, adapted to a Salpeter IMF in the mass range 0.1–100  $M_{\odot}$ ).

The comparison of the observed galaxy spectral energy distributions with models provides further constraints on the stellar populations contributing to the emerging radiation. Since we are interested in the *mean* stellar population(s) responsible for the relatively tight correlations of Figure 5, the zero-reddening flux density ratios reported in Table 5 can be used to create a *template* starburst spectrum (TSS) in the UV-to-NIR wavelength range. To improve the resolution in the wavelength range 0.125–1.0  $\mu\text{m}$ , the mean spectra of CKS94, rather than the broad band data of Table 5, are used for the TSS, after correction for reddening using the curve in Figure 6, and after the spectra are averaged to give a single zero-reddening template. The UV-optical template is therefore produced from a sample of 33 starbursts (CKS94), with a spectral resolution of 10  $\text{\AA}$ , and is normalized relatively to the *mean* K-band flux density using the  $F(0.70)/F(2.2)$  ratio as reference point. A direct comparison with the broad band data shows that the two sets of data are consistent with each other, and describe the same mean spectrum. Because of their resolution, the spectra from CKS94 provide detailed information on the far UV rise and the amplitude of the  $\sim 0.4 \mu\text{m}$  discontinuity, which may help constrain the stellar populations responsible for the observed radiation. The TSS is shown in Figure 13.

The spectral synthesis models of Bruzual & Charlot (1996, BC96 hereafter) are used

to generate spectra for the fit of the TSS. The adopted IMF is Salpeter in the mass range 0.1–100  $M_{\odot}$ . The BC96 models do not include the contribution from the nebular continuum emission, which we obtain from LH95 and add to the spectra produced by the BC96 code at the appropriate age. The BC96 models are given for solar metallicity only; this is sufficiently adequate for the present sample, where most of the galaxies have about solar metallicity. The synthetic spectrum to be compared with the TSS is built by combining three stellar populations of increasing age. The weights of the three populations are left as free parameters which are fitted via the minimum  $\chi^2$  technique. The best fit model must also satisfy the additional constrain of being able to reproduce the observed hydrogen line EWs. Of the three stellar populations, one is assumed to be young and responsible for most of the ultraviolet continuum (“star-forming population”); the other two are assumed to be older than the first and contribute mainly to the optical and IR continuum, to dilute the hydrogen line EWs (“underlying populations”). For this reason, the star-forming population is selected in the age range 0– $3 \times 10^7$  yr, and both the cases of an instantaneous burst of star formation and of a constant SFR regime are considered. The underlying populations have ages  $> 7 \times 10^7$  yr, and are produced by bursts of star formation. The latter is not a restrictive assumption if the the burst duration is finite, but much shorter than the age of the stars. A second type of fit of the TSS is also attempted by using only one star-forming population with constant SFR, and leaving the age as free parameter.

The spectrum produced by a star-forming population alone has systematically bluer colors than the TSS at UV wavelengths, for a stellar age of less than a few  $10^7$  yr. Figure 13a shows the example of a stellar population with constant SFR and  $2 \times 10^7$  yr old. This spectrum is clearly bluer than the TSS at all wavelengths. Among the instantaneous-burst populations, the one which comes closer to the TSS has an age of 10 Myr, still a much bluer UV spectrum, and far too red optical–IR colors. The TSS therefore appears to receive additional contribution from stellar populations which are older than a few times

$10^7$  yr. A starburst galaxy may indeed be conceived as a high-SFR event superimposed to an underlying quiescent galaxy, which is probably forming stars at a roughly constant (and small) rate since a Hubble time. In Figure 13b, this galaxy is modelled by the combination of two stellar populations: the first is undergoing star formation at a constant rate since  $1.5 \times 10^{10}$  yr and represents the underlying galaxy population; the second is undergoing star formation at a constant rate since  $2 \times 10^7$  yr and represents the starburst population. The fit of this model to the TSS is quite unsatisfactory, especially at optical wavelengths, where the model spectrum tends to be redder than the TSS. This is a common characteristics to all the synthetic spectra obtained by combining a relatively young population (age  $\sim 10^7$  yr or younger) with an old underlying population (age  $\sim 10^{10}$  yr).

A satisfactory fit of the TSS can be obtained with a stellar population characterized by constant SFR since  $1\text{--}2 \times 10^9$  yr (see Figure 13c). The low mass stars produced during this period of time, and which contribute mostly to the optical and IR flux, account approximately for the dilution of the EWs of the hydrogen emission lines, although a detailed comparison would imply an heavy extrapolation from the LH95 diagrams. The HI gas reservoir of our galaxies may be sufficient to support such long star formation timescales at the present SFR (columns 2 and 4 of Table 8). For Mrk 357, NGC 1614, NGC 4194, NGC 4385, NGC 6090, and Mrk 309, whose gas depletion timescale is shorter than  $10^9$  yr, the present burst of star formation is probably an exceptional event. However, molecular hydrogen has not been included in the gas supply estimates of Table 8, and, if present in large amounts, would considerably increase the depletion times. Rather than a single large star formation event lasting  $10^9$  yr, the starburst region subtended by our large aperture may be thought of as a collection of more modest bursting knots characterized by different values of the SFR and igniting at different epochs of the galaxy's life. A way to reduce the SFR and allow the burst to last longer with the available gas supply is to assume that low mass stars are not produced during bursts of star formation, or, alternatively, that the



IMF is flatter than Salpeter below a certain stellar mass; if the low mass limit for the IMF is  $1 M_{\odot}$ , instead of  $0.1 M_{\odot}$ , the SFRs decrease by a factor  $\sim 2.5$ , for  $\alpha=2.35$ . Whether this is the case in starburst galaxies is still debated (e.g., Rieke et al. 1980, 1993, Lester et al. 1990, Satyapal et al. 1995, BernLör 1993; see also below).

A better fit to the data in terms of  $\chi^2$  is given by the combination of three components: a  $2 \times 10^7$  yr population with constant SFR, and two intermediate age populations, generated by instantaneous bursts  $10^8$  yr and  $5 \times 10^8$  yr ago, respectively. They contribute 15%, 13%, and 72%, respectively, of the K-band flux (see Figure 13d). The intermediate age populations are responsible for the dilution of the EWs of the hydrogen emission lines, and account for the small values of the observed  $H\alpha$ ,  $Pa\beta$ , and  $Br\gamma$  EWs (see Table 7). An additional consistency check is to compare the K-band luminosities of the galaxies with the model. Column 7 of Table 8 gives for each galaxy the reddening corrected K-band luminosity,  $L_K$ , in units of the solar K-band luminosity, and normalized to the star formation rate SFR100; these values are to be compared with the quantity  $5.28 \times 10^9 L_{\odot} \text{ yr}/M_{\odot}$  derived for the model. Most of the galaxies lay within a factor two of the model value, and the median value for the observed  $L_K/\text{SFR100}$  is  $5.94 \times 10^9 L_{\odot} \text{ yr}/M_{\odot}$ . The exceptions are NGC 4861 and NGC 6217. As will be seen in a following section, the K-band flux of NGC 4861 receives about 50% contribution from the bursting population; in the case of NGC 6217, it is likely that old stellar populations provide the bulk of the K-band flux. The mass in stars per unit of SFR predicted by the model is  $1.62 \times 10^9 M_{\odot}$ . This value is also the timescale over which the stars have been produced, namely  $1.62 \times 10^9$  yr, if the SFR remained constant over that period of time; this is in rough agreement with the age of the oldest stellar population from the model ( $\approx 500$  Myr). If the star formation is episodic, some of the past episodes may have been characterized by different (possibly higher) values of the SFR, and the entire star-forming event by a different (possibly shorter) timescale. The amplitude of the discontinuity at  $0.4 \mu\text{m}$  in the synthetic model is overpredicted relative

to the observations; this characteristic remains true also when model fitting of individual galaxies is attempted (see below), and may be partially explained by the fact that the wavelength region 0.32–0.38  $\mu\text{m}$  is the noisiest in our spectra (cf. McQuade et al. 1995, Storchi-Bergmann et al. 1995). As already discussed above, underlying populations older than 1–2 Gyr produce increasingly worse fits of the TSS, mainly because the synthetic spectra are far too red at optical wavelengths; the underlying stellar population contributing to the mean starburst spectrum must thus be younger than  $\approx 2$  Gyr. Changing the metallicity of the model populations from solar to half solar (the typical value of our galaxies) has a negligible effect on this conclusion.

The small values of the hydrogen line EWs can be explained either as a dilution effect from an underlying population or as evidence for a high-mass-star truncated IMF. A 30  $M_{\odot}$  upper mass limit produces a factor 4–5 less ionizing photons than a 100  $M_{\odot}$  upper mass limit, for a Salpeter IMF (LH95), and therefore, smaller emission line EWs. For instance, a  $\sim 5 \times 10^7$  yr star-forming population, with constant SFR and a 0.1–30  $M_{\odot}$  Salpeter IMF, accounts for the observed mean EWs of Table 7. However, its spectrum does not reproduce other observables; it is, for instance, much bluer than the TSS (Figure 14). A fit of both the TSS and the line EWs with a high-mass truncated IMF still requires the presence of intermediate age underlying populations. In this case, the best fitting star-forming population has age 0.5– $1 \times 10^7$  yr, which is when red supergiants appear; a small change in age thus corresponds to a variation up to a factor 20 in the EW of the infrared hydrogen lines (LH95). This is in contradiction with the observational values of the  $\text{Br}\gamma$  EW, which show a small spread around the mean value. The model predicts a K-band luminosity per unit of  $\text{SFR}_{30} \sim 3.0 \times 10^9 L_{\odot} \text{ yr}/M_{\odot}$ , which is a factor  $\sim 2$  larger than the observed mean value  $L_K/\text{SFR}_{30} \simeq 1.4 \times 10^9 L_{\odot} \text{ yr}/M_{\odot}$ . This prediction is minimally dependent on the age of the star-forming population, since the intermediate age populations contribute more than 80% of the K-band flux, even when the red supergiants appear. The gas consumption

timescales decrease by a factor 4.35, going from  $M_{up}=100 M_{\odot}$  (cf. Table 8) to  $M_{up}=30 M_{\odot}$ ; for most of the galaxies in the sample the HI gas depletion time is, then, less than the age of the older population predicted by the model. There is, in conclusion, no compelling evidence for a high-mass-star truncated IMF from this set of data (see, also, Moffat 1996).

In summary, the TSS can be described either by a single star-forming population which is undergoing constant star formation since  $1\text{--}2\times 10^9$  yr, or by the combination of a relatively young ( $\sim 2\times 10^7$  yr), constant SFR population with two older underlying populations, in the age range  $10^8\text{--}10^9$  yr and no longer forming stars. The fitting technique is not sophisticated enough to break the two intermediate age populations into more components. It is interesting, however, that at least two intermediate age components, and maybe a continuously star-forming population, are needed to fit the observed spectrum; this support the idea that starburst activity in galaxies is spread over a timescale of roughly  $10^9$  yr and proceeds through episodes which may involve different but spatially close regions (e.g. Waller 1991). Stellar populations older than  $\sim 10^9$  yr are not needed to account for the TSS, implying that the emission from the most recently formed stars dominates the observed spectrum not only in the UV, but also at optical and IR wavelengths. This explains, a posteriori, why the continuum emission from the galaxies follows a common reddening trend at all wavelengths, as seen in section 4.1.

## 6.2. The Mass-to-Light Ratio

The best fit model to the TSS yields a stellar mass-to-light ratio,  $M/L_K$ , of  $0.31 M_{\odot}/L_{K,\odot}$ , where  $L_K$  is the K-band luminosity; 98.7% of the mass in this ratio is provided by the two intermediate age populations. The mean value of the observed mass-to-light ratio is  $1.44 M_{\odot}/L_{K,\odot}$  (see the last column of Table 8), or about 5 times

the stellar mass-to-light ratio predicted from the model. Each galaxy’s mass-to-light ratio has been derived from the dynamical mass,  $M_d$ , subtended by the observational aperture, using the HI velocity width from Huchtmeier & Richter (1989). The difference between the observed and the model mass-to-light ratios allows room for the presence of molecular and atomic gas, of stellar remnants and of low mass stars (older than  $\sim 2 \times 10^9$  yr) which contribute negligibly to the observed luminosity, but will contribute to the mass. An estimate of the HI mass contained within the observational aperture is given in column 6 of Table 8, and is in general a small fraction of the total mass within the aperture; the values of column 6 are derived assuming a spherical distribution for the HI gas. To estimate the contribution to the dynamical mass of the stars older than  $\sim 2 \times 10^9$  yr, we assume that the stellar populations follow a Hubble luminosity profile (Binney & Tremaine 1987). For a galaxy with typical stellar mass  $10^{11} M_\odot$  and radius 10 kpc, the mass contained within a region of 4 kpc in diameter is about  $3.6 \times 10^{10} M_\odot$ . This value is a factor 4 smaller if the galaxy follows an exponential profile. If the age of the stars is 10 Gyr or larger, the K-band luminosity produced by this low-mass star population is less than 15% of the observed mean value, and of the same order of magnitude of the observational uncertainties. The total mass produced by a star formation event lasting  $2 \times 10^9$  yr and with mean  $\text{SFR}_{100} = 9 M_\odot/\text{yr}$  (as derived from Table 6) is  $1.8 \times 10^{10} M_\odot$ , or about 1/2 of the pre-existing stars. Accounting for the mass returned to the ISM by supernova explosions would introduce a small difference in this estimate, because most of the mass is locked in low mass stars. The total stellar mass-to-light ratio is therefore 3 times larger than the mass-to-light ratio of the population generated by the star formation event, namely  $\sim 0.9 M_\odot/L_{K,\odot}$ . Only NGC 1614, NGC 4194, and NGC 4385 have mass-to-light ratios significantly smaller than  $0.9 M_\odot/L_{K,\odot}$ . A few reasons may explain their case: 1) the TSS does not match perfectly each individual spectral energy distribution, and specific stellar population models should be applied to individual galaxies; 2) the dynamical mass may be underestimated, because detailed density profiles

have not been taken into account.

In summary, the mean mass-to-light ratio derived from the observations is compatible with the value derived from the model. The implication is that an IMF with lower and upper mass limits in the range  $0.1\text{--}100\text{ M}_\odot$  can satisfactorily model the data, and a low-mass-stars deficient IMF is not required to explain the observations.

## 7. Individual Galaxies: NGC 7714 and NGC 4861

In order to test the effectiveness of our crude fitting technique, we try to reproduce the observed spectra of two galaxies: the starburst prototype NGC 7714 (Weedman et al. 1981), and the bluest galaxy in our sample, NGC 4861.

The spectrum of NGC 7714 (see Figure 15) is corrected for reddening using  $E(B-V)=0.4$  and the reddening values of Table 5 and CKS94. The best fit for the spectrum and the emission line EWs is given by a  $1\times 10^7$  yr population with constant SFR and two underlying populations with ages  $1\times 10^8$  yr and  $5\times 10^8$  yr. The flux from the three stellar populations accounts for 14%, 17% and 69%, respectively, of the K-band emission. The observed and predicted emission line EWs are shown in Table 7. The results from this model suggest that NGC 7714 has been experiencing episodic or continuous star formation over the last  $5\times 10^8\text{--}1\times 10^9$  yr, as already concluded by Gonzalez-Delgado et al. (1995). If the SFR were to remain constant over a period of  $10^9$  yr, the total mass produced by the star formation event would be  $\sim 6\times 10^9\text{ M}_\odot$ , comparable to the total HI mass in the galaxy. The K-band luminosity per unit of star formation rate and the stellar mass-to-light ratio predicted by the model are  $2.67\times 10^9\text{ L}_\odot\text{ yr/M}_\odot$  and  $0.32\text{ M}_\odot/\text{L}_\odot$ , respectively, to be compared with the values shown in Table 8. The observed M/L is about a factor 3.5 larger than the model M/L, implying that the use of an IMF with mass range  $0.1\text{--}100\text{ M}_\odot$  is

appropriate also for the case of NGC 7714. A low-mass-stars deficient IMF does not seem required for this galaxy, unlike previous results (Bernlöhr 1993, and references therein). Much of the difference between the present and previous conclusions on the IMF can be attributed to the reddening corrections adopted by different authors for the luminosity. If the dust and stars are assumed to be mixed (cf. Bernlöhr 1993), the reddening corrected luminosities will be larger, and the M/L values smaller, than those obtained by assuming that the dust is foreground to the stars (cf. Satyapal et al. 1995, for the case of M82). For instance, in a dust-star mixed geometry a measured  $E(B-V)=0.22$  at optical wavelengths corresponds to a K-band optical depth  $\tau_K = 2$  and the IR stellar continuum must be corrected for a reddening factor 2.3. In a foreground geometry the same value of the optical color excess corresponds to a K-band optical depth  $\tau_K = 0.06$  and to a reddening correction factor of only 1.06 for the IR stellar continuum.

NGC 4861 strongly deviates from the average behavior of the other galaxies: its spectrum is the bluest in our sample, and the EWs of its hydrogen emission lines are about one order of magnitude larger than the others (cf. Tables 2 and 3). NGC 4861 is the closest approximation to a pure starburst population in the present sample. After reddening correction, using the same recipe as for NGC 7714 and  $E(B-V)=0.2$ , the NGC 4861 spectrum is best fitted by the combination of a  $4 \times 10^6$  yr constant SFR population with a  $1.2 \times 10^{10}$  yr burst population (Figure 16a). The latter provides 52% of the K-band flux, 43% of the J-band flux, and 16% of the  $0.65 \mu\text{m}$  flux. However, this synthetic spectrum overpredicts the hydrogen line EWs, especially in the J and K bands (see model 1 in Table 7). If we impose that the star-forming population can only originate from an instantaneous burst of star formation, then the best fitting synthetic spectrum is given by a combination of a  $3 \times 10^6$  yr and a  $1.2 \times 10^{10}$  yr burst population (Figure 16b), where the latter provides 62% of the K-band flux, 52% of the J-band flux, and 18% of the  $0.65 \mu\text{m}$  flux. The  $\chi^2$  from the second model is about 30% worse than from the first model, but the

predicted values for the hydrogen line EWs are closer to the observed ones (see model 2 in Table 7). The EWs mismatch between model 1 and the observations could be alternatively explained if some of the ionized gas has been blown away from the observed galaxy region by stellar winds, so it does not contribute to the spectrum. Both model 1 and 2 are consistent with all the UV flux and most of the optical flux given by a very young stellar population, in the age range  $3\text{--}4 \times 10^6$  yr, in agreement with previous results (Barth et al. 1994). In both models, the optical continuum is overpredicted by  $\sim 25\text{--}30\%$ ; the observed optical spectrum may actually be underestimated, because the wavelength region  $0.32\text{--}0.45 \mu\text{m}$  is missing from the spectrum and a normalization cross-check between the UV and the optical spectra could not be performed. The use of solar metallicity models to reproduce the spectrum of this  $\sim 0.1 Z_{\odot}$  galaxy is not particularly relevant at this stage of the evolution and for the observables we are interested in, although it would matter at later stages, especially around  $10^7$  yr, when red supergiants appear (LH95).

The UV spectrum of NGC 4861 is slightly bluer than expected from models (cf. Figure 16); its spectral index is  $-2.85$ , to be compared with a theoretical index of  $-2.7$  for a young stellar population (LH95). Possibly, the galaxy UV spectrum is slightly overcorrected for reddening. NGC 4861, indeed, does not follow the mean reddening trend of the other galaxies in the sample (cf. Figure 5). For this reason, its spectrum was not used in the derivation of the obscuration curve or of the Template Starburst Spectrum. The reddening problem is only worsened by the use of the Galactic or LMC extinction curves, because these are steeper in the UV than the obscuration curve of Figure 6. In addition, the Galactic curve overcorrects the  $0.22 \mu\text{m}$  region (see Figure 16c). A more complex dust distribution than the foreground clumpy one adopted here may be present in this galaxy, although the reddening of the ionized gas does not provide evidence for such case (CKS96).

## 8. Conclusions

The analysis of the UV-to-NIR spectral energy distribution of 19 galaxies with starburst central regions shows that the reddening of the stars and of the ionized gas can be described by a foreground clumpy dust distribution, characterized by different covering factors in front of stars and gas. In the IR, the reddening of the stellar continuum is similar in value to that of the ionized gas, but the two values progressively diverge towards the UV. If a Galactic-type extinction curve is adopted for the gas, the UV-bright stars are about 60% less reddened than the nebular gas (cf. CKS94). In terms of a clumpy dust distribution, the radiation from the stellar continuum crosses, on average, 40% less dust clumps than the radiation from the gas. This difference can be understood if the dust, gas, and stars are not spatially coincident. The large observational aperture employed for the present sample covers the central 3–5 kpc in the galaxies, encompassing many regions at different evolutionary stages. Stellar winds and supernova explosions can create “holes” in the galaxy ISM through which UV-bright stars can shine. “Leaky” star-forming regions may be the source of ionization of the diffuse gas (Ferguson et al. 1996). OB stars have been found in field regions of galaxies, far enough from any bright HII region that they are likely to be born in situ (Wilson 1990, Massey et al. 1995). Young stars can be found in regions of very low density medium, unrelated to the brightest sources of nebular emission, and physically “detached” from the gas they ionize.

A departure from a foreground-equivalent dust distribution at wavelengths longer than  $2.2 \mu\text{m}$  is not excluded by the present results (cf. Puxley & Brand 1994), since opaque clouds become optically thin to the radiation of deeply embedded stars at sufficiently long wavelengths. IRAS data suggest, indeed, that a small fraction of the ionizing stars may be buried in optically thick clouds (Calzetti et al. 1995).

The reddening-corrected spectra and broad band flux densities of the sample galaxies



have been combined to form a “template starburst spectrum”. This spectrum, which is entirely derived from observational data, shows the mean intrinsic appearance, in wavelength space, of a starburst galaxy with 0.5–1 solar metallicity. The fit of the “template starburst spectrum” with stellar population models requires at least three different components: a star-forming population, which is responsible for most of the UV emission, and two intermediate age populations,  $1 \times 10^8$  yr and  $5 \times 10^8$  yr old, respectively, which contribute to a large fraction of the optical and IR emission. The star-forming component is producing stars at a constant rate since  $\sim 2 \times 10^7$  yr, in agreement with the age limits placed to this component by the current supernova rates, measured from the [FeII] emission line. The three stellar components which fit the “template starburst spectrum” are all relatively close in age and younger than  $10^9$  yr. Our fitting technique is not sophisticated enough to reveal whether more than three stellar components contribute to the mean spectrum, but the limiting case of continuous star formation over  $\sim 2 \times 10^9$  yr produces a synthetic spectrum which is still in general agreement with the observations. This suggests that starburst activity in galaxies is continuous but episodic (cf. Waller 1991) and covers relatively long periods of time, up to  $\sim 1$ – $2$  Gyr. Past star formation episodes have been as efficient as or more efficient than the present one at producing stars, and the star formation history of a starburst galaxy is characterized by events with different levels of star formation strength. The galaxy very old population (age  $\sim 10^{10}$  yr) does not contribute significantly to the template starburst spectrum, since the best fit models do not require components older than  $\sim 10^9$  yr. This is an “a posteriori” justification for the use of a foreground dust distribution to de-redden the galaxy spectra: stellar populations younger than  $\sim 10^9$  yr may have been generated during star formation episodes which are associated with the current event.

A Salpeter IMF with mass range  $0.1$ – $100 M_{\odot}$  has been adopted through the analysis. This assumption has been checked against various observables, and no obvious contradiction has been found. The observed galaxy mass-to-light ratios are compatible with a low mass

limit of about  $0.1 M_{\odot}$ , and there is no clear need for a low-mass-star deficient IMF. A high-mass-star truncated IMF is also in disagreement with the data; a Salpeter IMF in the range  $0.1\text{--}30 M_{\odot}$  can account for the small values of the nebular hydrogen line EWs, but produces a synthetic spectrum which is much bluer than the “template starburst spectrum”.

Spectral energy distributions of local galaxies are often compared with spectra or multi-band photometry of intermediate and high redshift galaxies in an effort to pin down the stellar composition, and therefore, the star formation history of the progenitors of present-day galaxies (e.g., Steidel et al. 1996, Madau et al. 1996). In this respect, the “template starburst spectrum” provides a baseline for comparisons with high-redshift star-forming galaxies, since it represents the the reddening-corrected UV-to-IR spectral energy distribution of a “typical” starburst galaxy, as derived from observations. However, metallicity differences may not be negligible between present-day and high-redshift galaxies, and comparisons should take this caveat into account.

The author would like to thank Tim Heckman for many discussions and useful suggestions while this work was taking shape; Anne Kinney for comments and constant encouragement; Claus Leitherer for providing the LH95 starburst models; Ron Allen, Ken Freeman, Nino Panagia, Jim Pringle, and Rosemary Wyse for a critical reading of the manuscript; Lee Armus for guidance through the infrared world. The author also acknowledges hospitality from the Observatories of the Carnegie Institute of Washington during part of the work. This research has made use of the NASA/IPAC Extragalactic Database (NED) which is operated by the Jet Propulsion Laboratory, California Institute of Technology, under contract with the National Aeronautics and Space Administration. Part of this research was supported by the NASA Grant NAGW-3757.

## REFERENCES

- Allen, R. J. 1996, in “New Extragalactic Perspectives in the New South Africa” (Kluwer: Dordrecht), D. L. Block & J. M. Greenberg eds., in preparation
- Armus, L., Shupe, D. L., Matthews, K., Soifer, B. T., Neugebauer, G. 1995, *ApJ*, 440, 200
- Balzano, V. A., & Weedman, D. W. 1981, *ApJ*, 243, 756
- Barth, C. S., Cepa, J., Vilchez, J. M., & Dottori, H. A. 1994, *AJ*, 108, 2069
- Beck, S. C., Turner, J. L., Ho, P. T., Lacy, J. H., & Kelly, D. M. 1996, *ApJ*, 457, 610
- Bernlöhr, K. 1993, *A&A*, 268, 25
- Black, J. H., & van Dishoeck, E. F. 1987, *ApJ*, 322, 412
- Bruzual, G. A., & Charlot, S. 1996, in preparation
- Binney, J., & Tremaine, S. 1987, *Galactic Dynamics* (Princeton University Press: Princeton), 39
- Boissé, P., & Thoraval, S. 1996, in “New Extragalactic Perspectives in the New South Africa” (Kluwer: Dordrecht), D. L. Block & J. M. Greenberg eds., in preparation
- Burstein, D., & Heiles, C. 1982, *AJ*, 87, 1165
- Byun, Y. I., Freeman, K. C., & Kylafis, N. D. 1994, *ApJ*, 432, 114
- Calzetti, D., Bohlin, R. C., Kinney, A. L., Storchi-Bergmann, T., & Heckman, T. M. 1995b, *ApJ*, 443, 136
- Calzetti, D., Kinney, A. L., & Storchi-Bergmann, T. 1994, *ApJ*, 429, 582
- Calzetti, D., Kinney, A. L., & Storchi-Bergmann, T. 1996, *ApJ*, 458, 132

- Campins, H., Rieke, G. H., & Lebofsky, M. J. 1985, *AJ*, 90, 896
- Carico, D. P., Sanders, D. B., Soifer, B. T., Matthews, K., & Neugebauer, G. 1990, *AJ*, 100, 70
- Carico, D. P., Soifer, B. T., Beichman, C., Elias, J. H., Matthews, K., & Neugebauer, G. 1986, *AJ*, 92, 1254
- Colina, L., Bohlin, R. C., & Castelli, F. 1996, *AJ*, in press
- Colina, L. 1993, *ApJ*, 411, 565
- Conti, P. S., & Vacca, W. D. 1994, *ApJ*, 423, L97
- De Boer, K. S., Jura, M. A., & Shull, M. J. 1987, in *Exploring the Universe with the IUE Satellite*, eds. Y. Kondo, W. Wamsteker, A. Boggess, M. Grewing, C. de Jager, A. L. Lane, J. L. Linsky, & R. Wilson (Reidel: Dordrecht), 485
- de Vaucouleurs, G., de Vaucouleurs, A., Corwin, H. G., Buta, R. J., Paturel, G., & Fouqué, P. 1991, *Third Reference Catalogue of Bright Galaxies (RC3)* (Springer Verlag: New York)
- De Young, D. S., & Heckman, T. M. 1994, *ApJ*, 431, 598
- Devereux, N. A. 1989, *ApJ*, 346, 126
- Dinerstein, H. L., & Shields, G. A. 1986, *ApJ*, 311, 45
- Disney, M., Davies, J., & Phillips, S. 1989, *MNRAS*, 239, 939
- Doyon, R., Puxley, P. J., & Joseph, R. D. 1992, *ApJ*, 397, 117
- Draine, B.T. 1990, in *The Evolution of the Interstellar Medium*, ed. L. Blitz, ASP Conference Series, 12, 193

- Draine, B. T., & Woods, D. T. 1990, *ApJ*, 363, 464
- Draine, B. T., Roberge, W.G., & Dalgarno, A. 1983, *ApJ*, 264, 485
- Elias, J. H., Frogel, J. A., Matthews, K., & Neugebauer, G. 1982, *AJ*, 87, 1029
- Ellis, T., Drake, R., Fowler, A. M., Gatley, I., Heim, J., Luce, R., Merrill, K. M., Probst, R., & Buchholz, N. 1992, in *Proceedings of SPIE*, 1765, 94
- Elson, R. A. W., Fall, S. M., & Freeman, K. C. 1989, *ApJ*, 336, 734
- Elston, R., & Maloney, P. 1990, *ApJ*, 357, 91
- Fanelli, M. N., O’Connell, R. W., & Thuan, T. X. 1988, *ApJ*, 334, 665
- Ferguson, A. N., Wyse, R. F. G., Gallagher, J. S., & Hunter, D. A. 1996, *AJ*, 111, 2265
- Fitzpatrick, E. L. 1986, *AJ*, 92, 1068
- Forbes, D. A., & Ward, M. J. 1993, *ApJ*, 416, 150
- Forbes, D. A., Ward, M. J., Rotaciuc, V., Blietz, M., Genzel, R., Drapatz, S., van der Werf, P. P., & Krabbe, A. 1993, *ApJ*, 406, L11
- Gilmore, G., & Wyse, R. F. G. 1988, *ApJ*, 367, L55
- Giovanelli, R., Haynes, M. P., Salzer, J. J., Wegner, G., Da Costa, L. N., & Freudling, W. 1995, *AJ*, 110, 1059
- Glass, I. S. 1981, *MNRAS*, 194, 795
- Goldader, J. D., Joseph, R. D., Doyon, R., & Sanders, D. B. 1995, *ApJ*, 444, 97
- Goldader, J. D., Joseph, R. D., Doyon, R., & Sanders, D. B. 1996, *ApJ*, submitted

- Gonzalez-Delgado, R. M., Perez, E., Diaz, A. I., Garcia-Vargas, M. L., Terlevich, E., & Vilchez, J. M. 1995, *ApJ*, 439, 604
- Graham, J. R., Wright, G. S., & Longmore, A. J. 1987, *ApJ*, 313, 847
- Greenhouse, M. A., Woodward, C. E., Thronson, H. A., Rudy, R. J., Rossano, G. S., Erwin, P., & Puetter, R. C. 1991, *ApJ*, 383, 164
- Greggio, L. 1996, in *The Interplay Between Massive Star Formation, the ISM and Galaxy Evolution*, (Edition Frontieres: France), D. Kunth, B. Guiderdoni, M. Heydari-Malayeri, & T. X. Thuan eds., 89
- Heckman, T.M., Armus, L., & Miley, G. 1990, *ApJS*, 74, 833
- Heckman, T. M., Krolik, J., Meurer, G., Calzetti, D., Kinney, A. L., Koratkar, A. P., Leitherer, C., Robert, C., & Wilson, A. 1995a, *ApJ*, 452, 549
- Heckman, T. M., Dahlem, M., Lehnert, M. D., Fabbiano, G., Gilmore, D., & Waller, W. H. 1995, *ApJ*, 448, 98
- Hodge, P. 1974, *ApJ*, 191, L21
- Hollenbach, D., & McKee, C. F. 1989, *ApJ*, 342, 306
- Hutchmeier, W. K., & Richter, O.-G. 1989, *A General Catalog of HI Observations of Galaxies* (Springer-Verlag New York Inc.)
- Hunter, D. A., & Gallagher, J. S. 1986, *PASP*, 98, 5
- Israel, F. P., & Koorneef, J. 1991, *A&A*, 250, 475
- Kawara, K., & Taniguchi, Y. 1993, *ApJ*, 410, L19

- Keel, W. C. 1993, in *Massive Stars: Their Lives in the Interstellar Medium*, ASP Conference Series, n. 35, J. P. Cassinelli & E. B. Churchwell eds., 498
- Kennicutt, R. C. 1983, *ApJ*, 272, 54
- Kinney, A. L., Bohlin, R. C., Calzetti, D., Panagia, N., & Wyse, R. F. G. 1993, *ApJS*, 86, 5
- Kinney, A. L., Calzetti, D., Bica, E. L., & Storchi-Bergmann, T. 1994, *ApJ*, 429, 172
- Kudritzki, R., Gabler, R., Kunze, D., Pauldrach, A. W. A., & Puls, J. 1991, in *Massive Stars in Starbursts* (Cambridge University Press: Cambridge), C. Leitherer, N. R. Walborn, T. M. Heckman, & C. A. Norman eds., 59
- Lançon, A., Rocca-Volmerange, B., & Thuan, T. X. 1996, *A&AS*, 115, 253
- Landini, M., Natta, A., Oliva, E., Salinari, P., & Moorwood, A.F.M. 1984, *A&A*, 134, 284
- Leitherer, C., & Heckman, T. M. 1995, *ApJS*96, 9
- Leitherer, C., Robert, C., & Drissen, L. 1992, *ApJ*, 401, 596
- Lester, D. F., Carr, J. S., Joy, M., & Gaffney, N. 1990, *ApJ*, 352, 544
- Madau, P., Ferguson, H. C., Dickinson, M. E., Giavalisco, M., Steidel, C. C., & Fruchter, A. 1996, *MNRAS*, in press
- Marlowe, A. T., Heckman, T. M., Wyse, R. F. G., & Schommer, R. 1995, *ApJ*, 438, 563
- Massey, P., Lang, C.C., De Gioia-Eastwood, K., & Garmany, C.D. 1995, *ApJ*, 438, 188
- Mayya, Y. D., & Prabhu, T. P. 1996, *AJ*, in press
- McQuade, K., Calzetti, D., & Kinney, A. L. 1995, *ApJS*, 97, 331

- Meurer, G. R., Heckman, T. M., Leitherer, C., Kinney, A. L., Robert, C., & Garnett, D. R. 1995, *AJ*, 110, 2665
- Moffat, A. F. J. 1996, proceedings of the meeting “Starburst Activity in Galaxies”, Puebla (Mexico), J. Franco, R. Terlevich, and G. Tenorio-Tagle eds.
- Moorwood, A. F. M., & Oliva, E. 1988, *A&A*, 203, 278
- Moorwood, A. F. M., & Oliva, E. 1990, *A&A*, 239, 78
- Moorwood, A. F. M., & Oliva, E. 1994, *ApJ*, 429, 602
- Mouri, H. 1994, *ApJ*, 427, 777
- Mouri, H., Kawara, K., & Taniguchi, Y. 1993, *ApJ*, 406, 52
- Natta, A., & Panagia, N. 1984, *ApJ*, 287, 228
- Nussbaumer, H., & Storey, P. J. 1988, *A&A*, 193, 327
- O’Connell, R. W., Gallagher, J. S., & Hunter, D. A. 1994, *ApJ*, 433, 65
- Oliva, E., Moorwood, A. F. M., & Danziger, I. J. 1989, *A&A*, 214, 307
- Osterbrock, D. E., 1989, *Astrophysics of Gaseous Nebulae*, Univ. Science Books
- Panagia, N. 1978, in *Infrared Astronomy*, G. Setti & G. G. Fazio eds. (Reidel: Dordrecht), 115
- Puxley, P. J., & Brand, P. W. J. L. 1994, *MNRAS*, 266, 431
- Puxley, P. J., Hawarden, T. G., & Mountain, C. M. 1990, *ApJ*, 364, 77
- Puxley, P. J., Lumsden, S. L., Brand, P. W. J. L., & Doyon, R. 1994, *MNRAS*, 270, 7P
- Ratnatunga, K. U., & van den Bergh, S. 1989, *ApJ*, 343, 713



- Rieke, G. H., Lebofsky, M. J., Thompson, R. I., Low, F. J., & Tokunaga, A. T. 1980, *ApJ*, 238, 24
- Rieke, G. H., Cutri, R. M., Black, J. H., Kailey, W. F., McAlary, C. W., Lebofsky, M. J., & Elston, R. 1985, *ApJ*, 290, 116
- Rieke, G. H., Loken, K., Rieke, M. J., & Tamblyn, P. 1993, *ApJ*, 412, 99
- Satyapal, S., Watson, D. M., Pipher, J. L., Forrest, W. J., Coppenbarger, D., Raines, S. N., Libonade, S., Piché, F., Greenhouse, M. A., Smith, H. A., Thompson, K. L., Fischer, J., Woodward, C. E., & Hodge, T. 1995, *ApJ*, 448, 611
- Scoville, N. Z., Matthews, K., Carico, D. P., & Sanders, D. B. 1988, *ApJ*, 327, L71
- Seaton, M. J. 1979, *MNRAS*, 187, 73P
- Shields, J. C. 1993, *ApJ*, 419, 181
- Shields, J. C., & Kennicutt, R. C. 1995, *ApJ*, 454, 807
- Shlosman, I. 1992, in *Relationships between Active Galactic Nuclei and Starburst Galaxies* (San Francisco: ASP), A. V. Filippenko ed., 335
- Shull, J. M., & Draine, B. T., in *Interstellar Processes*, eds. D. Hollenbach & H. Thronson (Reidel: Dordrecht), 283
- Stasinska, G. & Leitherer, C. 1996, *ApJS*, 107, in press.
- Steidel, C. C., Giavalisco, M., Pettini, M., Dickinson, M., & Adelberger, K. L. 1996, *ApJ*, 462, L17
- Sternberg, A., & Dalgarno, A. 1989, *ApJ*, 338, 197
- Storchi-Bergmann, T., Calzetti, D., & Kinney, A. L. 1994, *ApJ*, 429, 572

- Storchi-Bergmann, T., Kinney, A. L., & Challis, P. 1995, *ApJS*, 98, 103
- van den Bergh, S., & Tamman, G. A. 1991, *ARAA*, 29, 363
- van der Werf, P. P., Genzel, R., Krabbe, A., Blietz, M., Lutz, Drapatz, S., Ward, M. J., & Forbes, D. A. 1993, *ApJ*, 405, 522
- Waller, W. H. 1991, *ApJ*, 370, 144
- Weedman, D. W., Felman, F. R., Balzano, V. A., Ramsey, L. W., Sramek, R. A., & Wu, C.-C. 1981, *ApJ*, 248, 105
- Wilson, C. D. 1990, *AJ*, 101, 1663
- Witt, A. N., Thronson, H. A., & Capuano, J. M. 1992, *ApJ*, 393, 611
- Witt, A. N., & Gordon, K. D. 1996, *ApJ*, 463, 681
- Xu, C., & Buat, V. 1995, *A&A*, 293, L65

Fig. 1 – Infrared spectra at J (left panels) and K (right panels) of 10 galaxies in the sample. The ordinate axis is the flux density  $F(\lambda)$  in units of  $10^{15}$  erg/s/cm<sup>2</sup>/Å. The position of the emission lines [FeII] (1.257  $\mu$ m), Pa $\beta$  (1.282  $\mu$ m), H<sub>2</sub>  $v = 1 - 0S(1)$  (2.121  $\mu$ m), and Br $\gamma$  (2.166  $\mu$ m) is indicated for the nearby galaxy NGC 1569 and for the distant galaxy NGC 1614. None of the emission lines is resolved. The spectra have been smoothed by a 3 pixel boxcar.

Fig. 2 – Two examples of ultraviolet, optical, and near-infrared spectra with no normalization between the three wavelength ranges. The galaxies are NGC 1614 and NGC 7714. The flux density is in erg/s/cm<sup>2</sup>/Å and is plotted as a function of the wavelength  $\lambda$  in the range 1,200–22,500 Å.

Fig. 3 – The spectral index  $\beta_{im}$  derived from the J, H, and K images versus the index  $\beta_{sp}$  derived from the NIR spectra. The  $1\sigma$  error bars are shown for each point. As expected, the data follow a straight line with slope unity. IC 1586 and Mrk 542 are exceptions to this trend (see text).

Fig. 4 – The color-color diagram for the 24 galaxies in the sample. The values are corrected for the foreground Galactic extinction. The open squares are the 19 starburst galaxies and the filled squares are the Seyfert 2s NGC262, NGC1275, NGC1667 and the LINER NGC6764, with photometry obtained in a 10'' circular aperture (Table 1); the position of NGC4861 is labelled. The filled triangles mark the trajectory of the colors of NGC 1068 for increasing extraction apertures (in the direction indicated by the arrow). The apertures are 5'', 10'', 15'', 20'', 30'', and 40''. The maximum value of the aperture, 40'', is set by the contrast of the image relative to the background. The infrared colors of an annulus with internal and external radii of 15'' and 30'', respectively, centered on the peak

of the emission in NGC 1068 are also shown (filled circle).

Fig. 5 – The stellar continuum ratios  $\log[F(0.16)/F(2.18)]$  (left panel) and  $\log[F(1.29)/F(2.18)]$  (right panel) are plotted as a function of the color excess measured from  $H\beta/Br\gamma$ . The typical  $1\sigma$  uncertainties on the data are shown in the lower left corner of the figures. The linear fit to the data, discussed in the text, is also shown. The positions of NGC4861 and IC1586 are marked in the left and right panels, respectively, and are not included in the fits of the data.

Fig. 6 – The obscuration curve derived from the stellar continuum flux densities of the starburst galaxies in the sample. The vertical axis shows the difference  $k'(\lambda) - k'(2.2)$ , where the K-band ( $2.2\mu\text{m}$ ) flux densities are the selected reference values. The horizontal axis is  $\log \lambda(\mu\text{m})$ . The filled circles are from the  $E(B-V)_{H\alpha/H\beta}$  fits; the filled triangles are from the  $E(B-V)_{H\beta/Br\gamma}$  fits. The  $1\sigma$  uncertainties are reported. The obscuration curve derived by CKS94 is overlapped, with the V-band value arbitrarily chosen to be  $k'(0.55) - k'(2.2) = 2$  (continuous line).

Fig. 7 – The observed flux density ratios at UV, optical and IR for the 19 starburst galaxies (filled dots). The typical  $1\sigma$  uncertainty on the data is shown at the bottom-right corner of the plot. The two curved lines represent synthetic flux density ratios as derived from models of stellar populations, as a function of the age of the population. The arrows on the curves indicate the direction of increasing age. The dotted curve shows the colors of an aging population, originated from an instantaneous burst of star formation, in the age range  $1 \times 10^7 - 5 \times 10^8$  yr. The dot-dashed curve show the colors of a stellar population with constant star formation rate in the age range  $1 \times 10^7 - 1.5 \times 10^{10}$  yr. The straight lines represent the reddening trends, as derived from the CKS94 obscuration

curve (continuous lines), from the Galactic extinction (dashed line), and from the LMC extinction (long-short dashed line). The reddening increases from left to right. The intrinsic colors,  $[F_{\odot}(0.55)/F_{\odot}(0.16); F_{\odot}(2.2)/F_{\odot}(0.16)]$ , are derived from the Template Starburst Spectrum (see Figure 13 and section 6). The positions of NGC 4861 and IC 214 are indicated.

Fig. 8 – The color excess  $E(B-V)$  derived from the hydrogen Balmer/Brackett line ratio,  $H\beta/Br\gamma$ , is shown as a function of the color excess from the Balmer line ratio,  $H\alpha/H\beta$ . The error bars are  $1\sigma$  uncertainties. Models of foreground clumpy dust are overplotted to the data; in the scattering model, the radiation along the line of sight includes scattered light from sources outside the observational beam (dashed line); in the non-scattering model, the scattered light does not contribute to the observed radiation (continuous line). The models are shown for an average of  $\mathcal{N}=10$  and  $\mathcal{N}=1000$  clumps along the line of sight.

Fig. 9 – The selective obscuration produced by a foreground distribution of dust clumps with: (1)  $\tau_c(0.55) = 0.37$  and  $f = \mathcal{N}^s/\mathcal{N}^g = 1$ , using both the Galactic (1G) and the LMC (1L) extinction curves; (2)  $\tau_c(0.55) = 0.37$  and  $f = 0.6$  (2G and 2L); (3)  $\tau_c(0.55) = 0.17$  and  $f = 0.6$  (3G and 3L). The parameter  $f = 0.6$  implies that the stellar continuum radiation crosses 60% of the dust clumps crossed by the nebular radiation. The value of the clump optical depth  $\tau_c(0.55) = 0.37$  corresponds to  $E(B-V)_{H\alpha/H\beta}=0.90$  and  $E(B-V)_{H\beta/Br\gamma}=1.0$ ;  $\tau_c(0.55) = 0.17$  corresponds to  $E(B-V)_{H\alpha/H\beta}=0.51$  and  $E(B-V)_{H\beta/Br\gamma}=0.54$ , for  $\mathcal{N}^g=10$ .

Fig. 10 – The  $H_2$   $v=1-0$   $S(1)(2.212\ \mu\text{m})/Br\gamma(2.166\ \mu\text{m})$  ratio as a function of  $[FeII](1.257\ \mu\text{m})/Pa\beta(1.282\ \mu\text{m})$ . The positions of the LINER galaxy NGC 6764 and of the two starbursts NGC 4861 and NGC 1569 are shown. Corrections for the dust reddening are negligible, and were not applied.

Fig. 11 – The  $\text{H}_2$   $v=1-0$   $\text{S}(1)$  ( $2.212 \mu\text{m}$ ) line flux as a function of the  $\text{Br}\gamma$  ( $2.166 \mu\text{m}$ ) flux for the starburst galaxies. The lines are corrected for the effects of both foreground and intrinsic reddening using the values of the color excess from column 4 of Table 1, and from the  $\text{H}\beta/\text{Br}\gamma$  ratios (see Table 4), respectively. The  $1 \sigma$  uncertainties are reported.

Fig. 12 – As Figure 11, now for the  $[\text{FeII}]$  ( $1.257 \mu\text{m}$ ) and the  $\text{Pa}\beta$  ( $1.282 \mu\text{m}$ ) line fluxes.

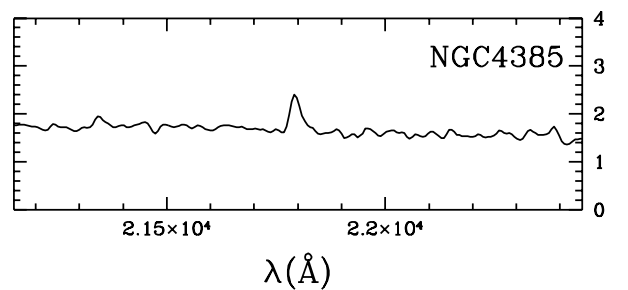
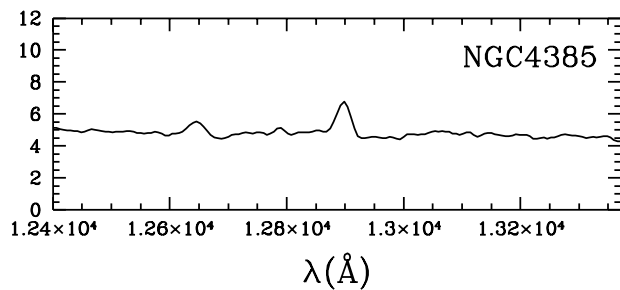
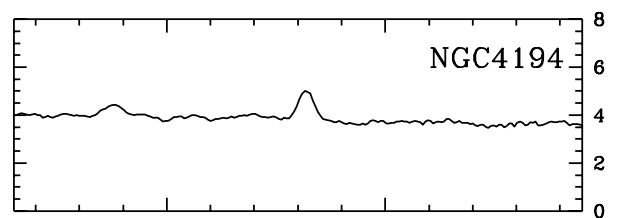
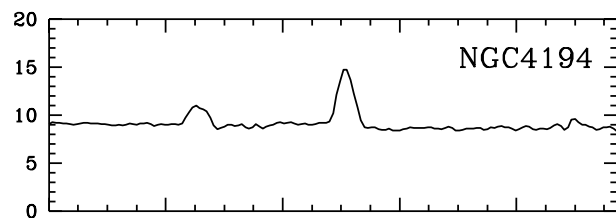
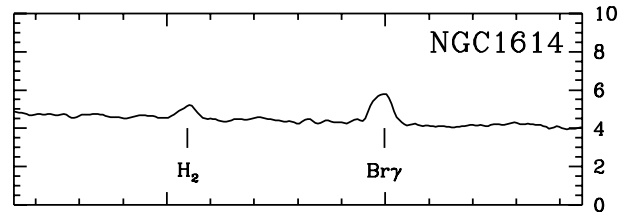
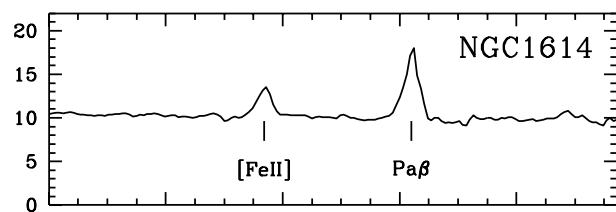
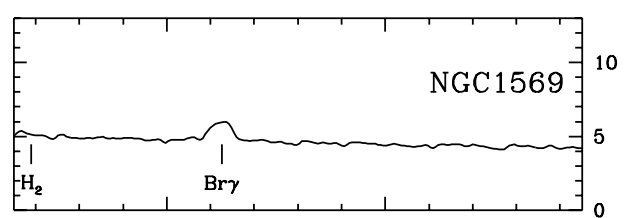
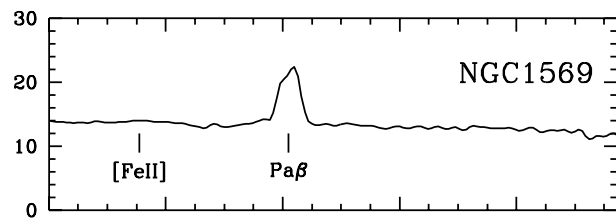
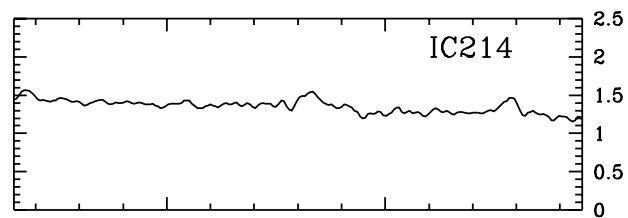
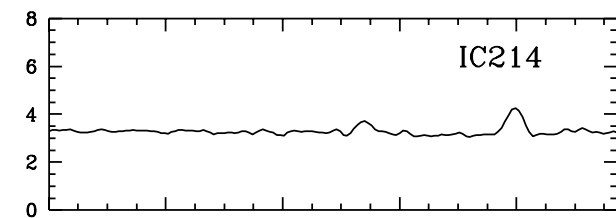
Fig. 13 – The template starburst spectrum (TSS), in units of flux density as a function of wavelength, in the range  $0.125\text{--}2.2 \mu\text{m}$ . The spectrum is normalized to the K-band flux density,  $F(2.2)$ . The error bar at the bottom left corner of each panel gives a measure of the typical  $1 \sigma$  uncertainty. The spectrum covers continuously the range  $0.125\text{--}1.0 \mu\text{m}$  (solid line); the two filled circles are the flux density values in the J and H bands. In each panel, the template is overlapped to synthetic spectra (dotted lines) produced from the Bruzual & Charlot’s (1996) and Leitherer & Heckman (1995) models, with Salpeter IMF in the range  $0.1\text{--}100 M_\odot$ . The synthetic spectra are given by: a) a  $2 \times 10^7$  yr population with constant SFR; b) the combination of two populations with constant SFR, the first  $2 \times 10^7$  yr old, and the second  $1.5 \times 10^{10}$  yr old; c) a  $2 \times 10^9$  yr population with constant SFR; d) a composite model made of a constant SFR,  $2 \times 10^7$  yr old population, and two underlying populations,  $1 \times 10^8$  yr and  $5 \times 10^8$  yr old, and both generated by an instantaneous burst of star formation; the contribution of each component is also shown, going from the blue 20 Myr population (dashed line), to the 100 Myr population (dot-dashed line), to the red 500 Myr population (long-dashed line).

Fig. 14 – The TSS (solid line + filled circles) is overplotted to the synthetic spec-

trum of a  $5 \times 10^7$  yr population with constant SFR, and a Salpter IMF in the mass range  $0.1\text{--}30 M_{\odot}$  (dotted line). The scale and the axis labels are the same as in Figure 13.

Fig. 15 – The spectrum of NGC 7714 (solid line for the UV and optical continuum + filled circles for the J and H band flux densities), dereddened using the recipe of section 4.1, is overlapped to the best fitting synthetic spectrum (dotted line), given by the combination of a  $1 \times 10^7$  yr population with constant SFR, plus two underlying populations,  $1 \times 10^8$  yr and  $5 \times 10^8$  yr old, respectively, and originated from an instantaneous burst of star formation (see text). The axis labels are as in Figure 13.

Fig. 16 – The spectrum of NGC 4861 (solid line for the UV and optical continuum + filled circles for the J and H band flux densities), dereddened using the recipe of section 4.1, is overplotted to best fitting synthetic spectra (dotted lines): a) a  $4 \times 10^6$  yr, constant SFR population with a  $1.2 \times 10^{10}$  yr burst population; b) two burst populations, one  $3 \times 10^6$  yr old and the other  $1.2 \times 10^{10}$  yr old. c) The spectrum of NGC 4861 is dereddened using two different methods: the recipe of section 4.1 (solid line) and the Galactic extinction curve (dotted line). The axis labels are as in Figure 13.





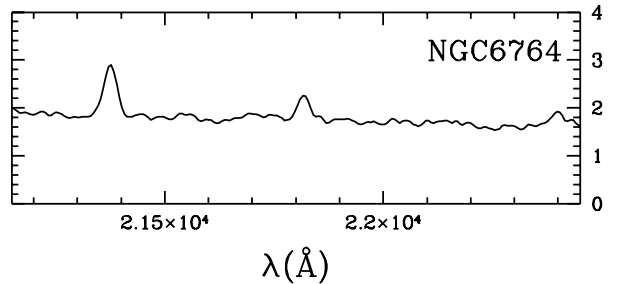
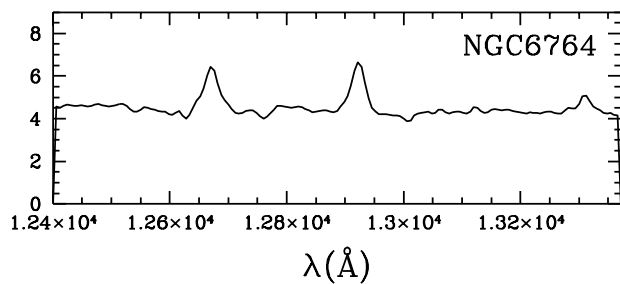
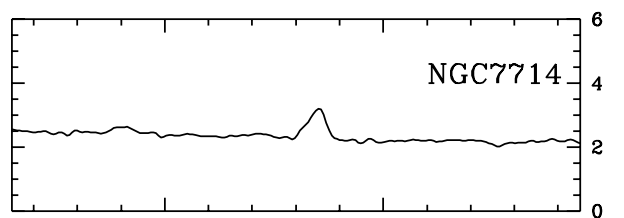
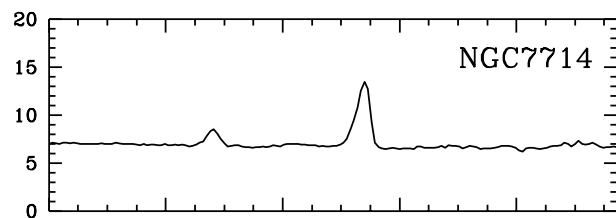
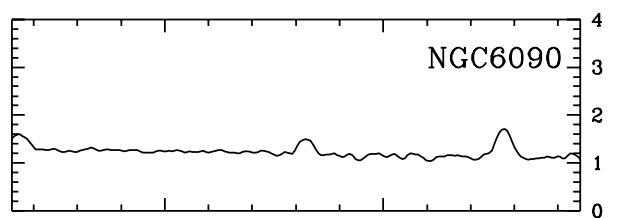
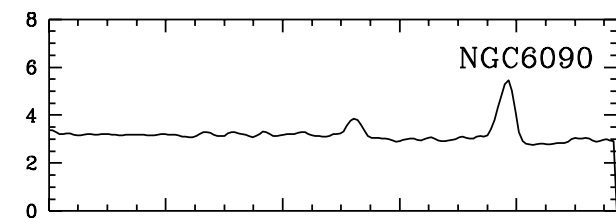
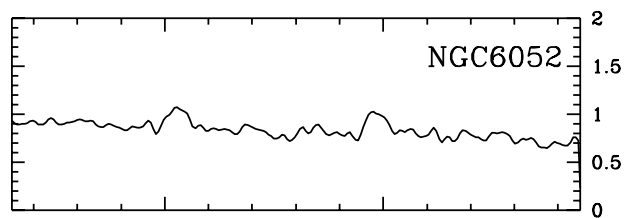
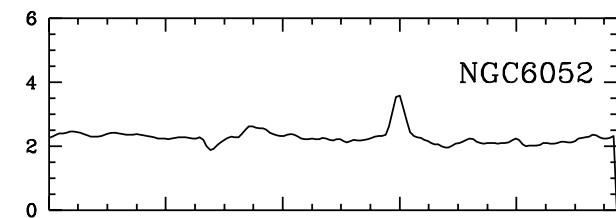
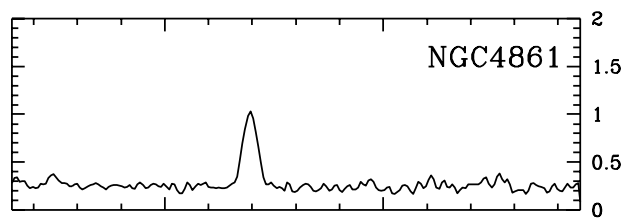
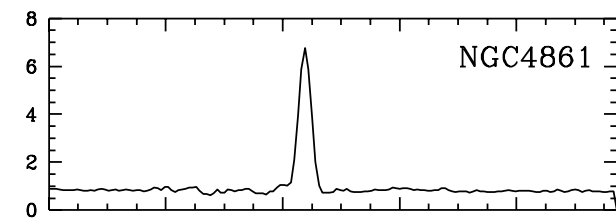


TABLE 1  
INFRARED PHOTOMETRY IN  $10''$  CIRCULAR APERTURE

Galaxy	Type <sup>a</sup>	$z^b$	$E(B-V)_G^c$	K	J-H	H-K
IC1586	SB	0.020	0.02	12.45	0.67	0.30
NGC262	Sy2	0.015	0.06	11.50	0.70	0.42
Haro15	SB	0.021	0.02	12.68	0.58	0.32
Mrk357	SB	0.053	0.04	13.28	0.63	0.51
IC214	SB	0.032	0.03	11.52	0.74	0.47
NGC1068	Sy2	0.004	0.01	7.06	0.90	1.16
NGC1140	SB	0.005	0.03	11.58	0.60	0.23
NGC1275	Sy2	0.017	0.17	10.68	0.69	0.44
NGC1569	SB	0.000	0.51	10.58	0.52	0.18
NGC1614	SB	0.016	0.05	10.16	0.80	0.53
NGC1667	Sy2	0.015	0.05	10.75	0.73	0.32
NGC4194	SB	0.008	0.00	10.21	0.70	0.42
NGC4385	SB	0.007	0.02	11.28	0.64	0.37
NGC4861	SB	0.003	0.00	13.13	0.38	0.29
NGC5860	SB	0.017	0.01	11.96	0.67	0.25
NGC6052	SB	0.015	0.03	12.11	0.59	0.29
NGC6090	SB	0.029	0.00	11.56	0.68	0.45
NGC6217	SB	0.005	0.04	10.53	0.68	0.35
NGC6764	LINER	0.008	0.06	11.22	0.70	0.39
NGC7250	SB	0.004	0.15	12.11	0.57	0.26
NGC7673	SB	0.010	0.04	11.98	0.56	0.27
NGC7714	SB	0.009	0.04	10.87	0.63	0.35
Mrk309	SB	0.042	0.05	12.58	0.64	0.47
Mrk542	SB	0.024	0.02	12.69	0.61	0.33

<sup>a</sup> Activity type: SB=starburst, Sy2=Seyfert 2.

<sup>b</sup> Redshift.

<sup>c</sup> Foreground Galactic color excess.

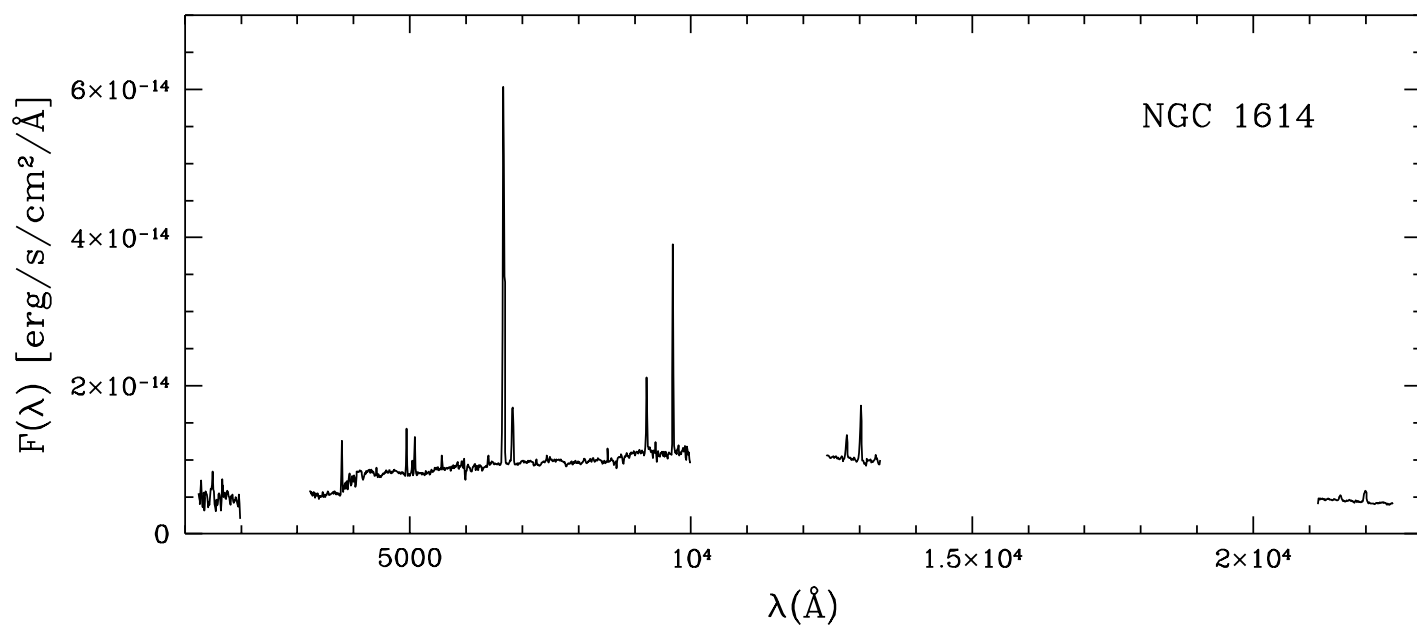
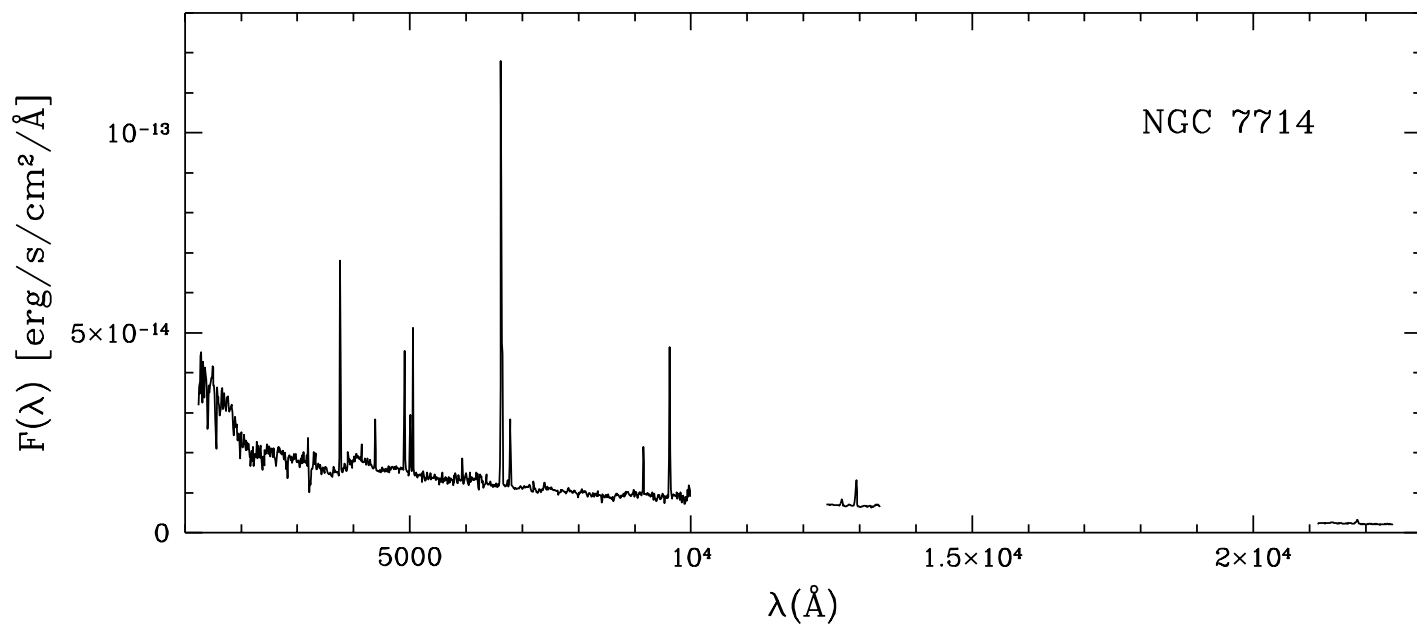


TABLE 2  
DERIVED QUANTITIES FROM UV, OPTICAL AND INFRARED DATA

Galaxy	E(B-V) <sup>a</sup> $H\alpha/H\beta$	$\log(O/H) + 12$ <sup>b</sup>	EW(H $\alpha$ ) <sup>c</sup> Å	$10^{15} \times F(0.16)$ <sup>d</sup> erg/s/cm <sup>2</sup> /Å	$10^{15} \times F(0.55)$ <sup>e</sup> erg/s/cm <sup>2</sup> /Å	$10^{15} \times F(2.2)$ <sup>f</sup> erg/s/cm <sup>2</sup> /Å	$\beta_{im}$ <sup>g</sup>
IC1586	0.57	8.53	72.8	6.20	3.94	0.40	-1.94
Haro15	0.00	8.57	95.5	20.91	4.37	0.38	-2.08
Mrk357	0.12	8.53	322.3	15.88	1.67	0.18	-1.77
IC214	0.53	8.68	82.5	7.60	2.36	1.15	-1.58
NGC1140	0.10	8.51	130.2	52.52	15.21	0.92	-2.16
NGC1569	0.06	8.37	89.3	417.00	92.35	3.63	-2.32
NGC1614	0.93	8.84	120.2	7.20	10.07	3.82	-1.43
NGC4194	0.79	8.81	94.5	15.00	16.84	3.26	-1.73
NGC4385	0.60	8.65	90.3	16.20	8.35	1.45	-1.99
NGC4861	0.20	8.30	945.8	86.48	3.17	0.23	-2.43
NGC5860	0.69	9.24	50.5	7.01	6.83	0.75	-1.97
NGC6052	0.20	8.61	80.3	15.01	8.85	0.76	-2.10
NGC6090	0.59	8.77	157.3	10.19	5.11	1.06	-1.72
NGC6217	0.53	8.98	52.8	21.88	14.08	2.69	-1.88
NGC6764	...	...	...	...	...	...	-1.79
NGC7250	0.05	8.65	89.7	35.61	7.64	0.58	-2.21
NGC7673	0.42	8.48	76.2	26.90	10.73	0.83	-2.17
NGC7714	0.39	8.71	191.0	44.71	15.40	1.93	-1.93
Mrk309	0.63	9.19	65.3	3.24	2.49	0.39	-1.66
Mrk542	0.29	8.87	40.1	6.91	2.85	0.35	-2.02

<sup>a</sup>Intrinsic color excess, from H $\alpha$ /H $\beta$  emission line ratio. The optical emission lines are corrected for the underlying stellar absorption (CKS94).

<sup>b</sup>Oxygen abundance. For reference, the adopted solar value is  $\log(O/H)+12=8.9$

<sup>c</sup>Equivalent width of the H $\alpha$  emission line.

<sup>d</sup>Mean flux density in the range 0.125–0.195  $\mu$ m, centered at 0.16  $\mu$ m, from the IUE spectra.

<sup>e</sup>Mean flux density in the range 0.505–0.595  $\mu$ m, centered at 0.55  $\mu$ m, from the optical spectra.

<sup>f</sup>Flux density at 2.2  $\mu$ m, from the IR images.

<sup>g</sup>NIR spectral slope, from the images.

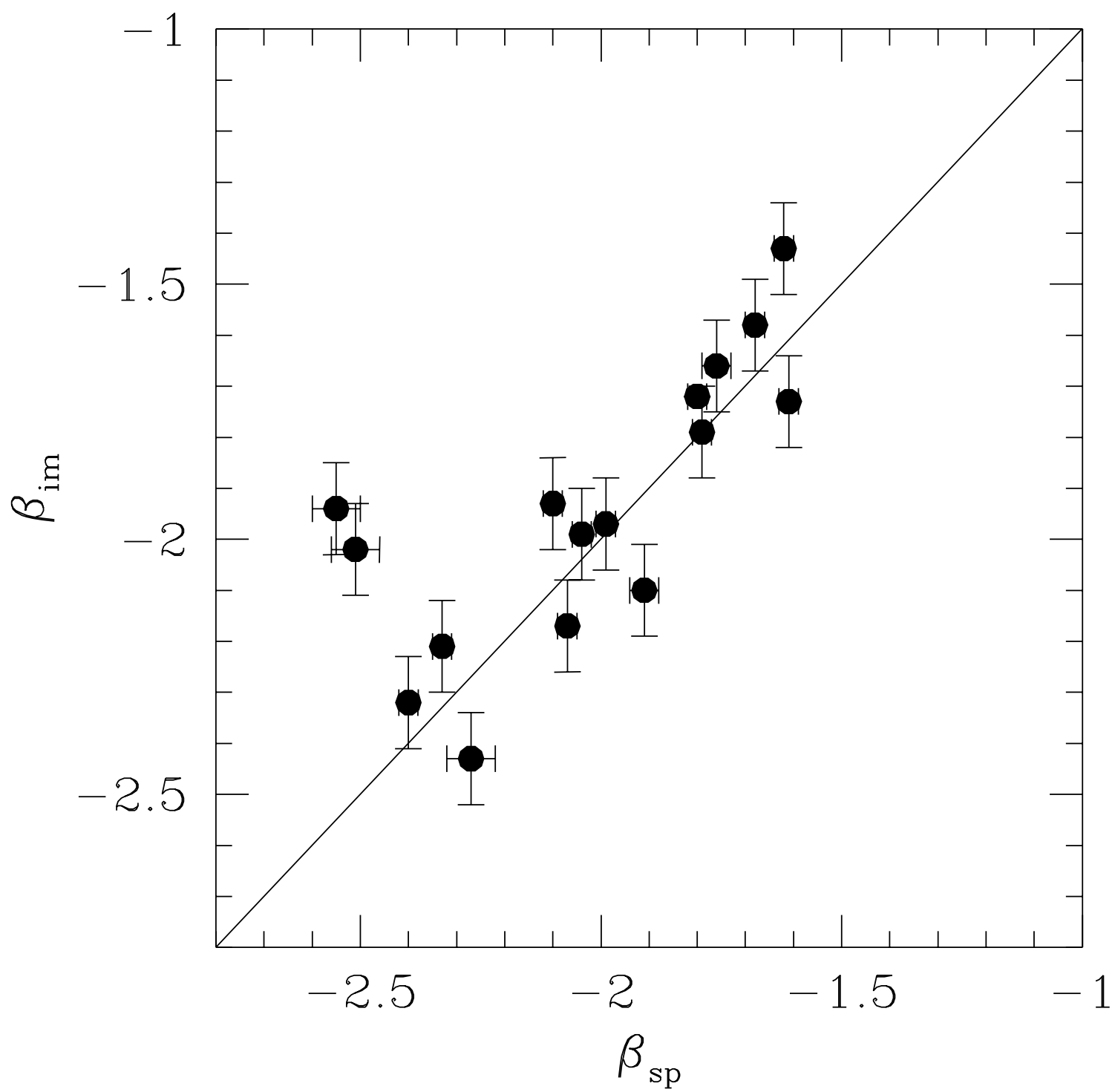


TABLE 3  
OBSERVATIONAL DATA FROM THE NIR SPECTRA

Galaxy	$10^{14} P_{a\beta}$ (1.28 $\mu\text{m}$ ) <sup>a</sup> erg/s/cm <sup>2</sup>	EW( $P_{a\beta}$ ) <sup>b</sup> Å	$10^{14} Br\gamma$ (2.17 $\mu\text{m}$ ) <sup>a</sup> erg/s/cm <sup>2</sup>	EW( $Br\gamma$ ) <sup>b</sup> Å	$10^{14}$ [FeII] (1.26 $\mu\text{m}$ ) <sup>a</sup> erg/s/cm <sup>2</sup>	$10^{14}$ H <sub>2</sub> (2.12 $\mu\text{m}$ ) <sup>a</sup> erg/s/cm <sup>2</sup>
IC1586	1.65±0.12	12.0	0.52±0.11	14.0	0.99±0.11	0.38±0.09
IC214	4.25±0.30	13.8	0.91±0.08	7.3	1.65±0.17	0.93±0.19
NGC1569	33.13±1.65	24.9	7.16±0.36	15.2	0.94±0.38	0.40±0.20
NGC1614	22.31±0.45	23.2	7.90±0.71	18.4	10.50±0.53	2.87±0.29
NGC4194	19.51±0.59	22.1	5.25±0.26	13.9	7.45±0.45	2.32±0.26
NGC4385	6.60±0.33	14.4	2.47±0.32	15.4	2.97±0.33	0.62±0.16
NGC4861	15.57±0.31	199.0	3.05±0.18	122.5	0.20±0.10	0.28±0.10
NGC5860	2.35±0.24	8.6	0.77±0.20	8.0	0.58±0.08	0.35±0.10
NGC6052	3.97±0.28	17.8	1.17±0.18	15.1	1.10±0.20	1.05±0.19
NGC6090	8.17±0.25	28.1	2.51±0.15	22.4	2.26±0.23	1.23±0.15
NGC6764	6.73±0.67	15.6	1.54±0.12	8.7	7.09±0.71	4.03±0.16
NGC7250	4.58±0.37	20.6	0.97±0.12	15.1	1.17±0.29	0.15±0.12
NGC7673	5.37±0.32	17.0	1.13±0.19	10.6	1.49±0.21	0.62±0.12
NGC7714	19.30±0.58	29.0	4.99±0.20	22.3	4.55±0.27	1.25±0.15
Mrk309	1.53±0.31	14.0	...	...	...	...
Mrk542	1.25±0.31	9.9	...	...	...	...

<sup>a</sup>The quoted error bars are statistical 1  $\sigma$  uncertainties.

<sup>b</sup>Equivalent Width.

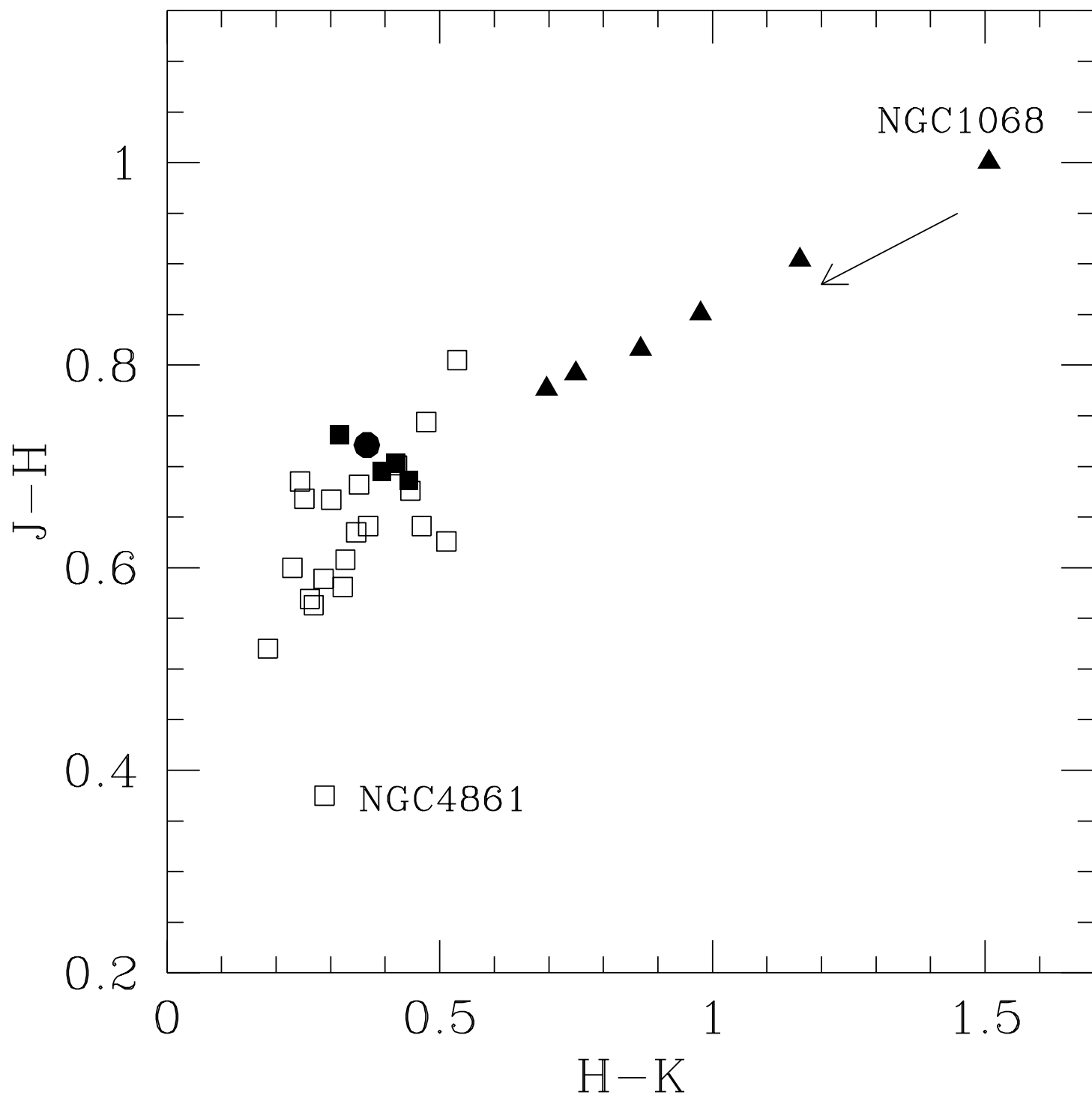


TABLE 4  
DERIVED QUANTITIES FROM THE NIR SPECTRA

Galaxy	E(B-V) $H\beta/Br\gamma$	$10^{15} \times F(2.18)^a$ erg/s/cm <sup>2</sup> /Å	$\beta_{sp}^b$	[FeII]/H <sub>2</sub> <sup>c</sup>	H <sub>2</sub> (2.22)/H <sub>2</sub> (2.12) <sup>d</sup>
IC1586	0.41±0.08	0.37	-2.55	4.8±1.6	...
IC214	0.70±0.05	1.34	-1.68	2.2±0.6	...
NGC1569	0.13±0.04	5.23	-2.40	2.9±1.9	< 0.35
NGC1614	0.97±0.04	4.45	-1.62	7.6±1.0	...
NGC4194	0.65±0.04	3.82	-1.61	5.0±0.7	~ 0.16 <sup>e</sup>
NGC4385	0.52±0.05	1.66	-2.04	10.5±2.5	< 0.42
NGC4861	0.20±0.04	0.25	-2.27	0.9±0.5	< 0.26
NGC5860	0.61±0.10	0.99	-1.99	3.2±1.2	...
NGC6052	0.29±0.06	0.83	-1.91	1.8±0.6	...
NGC6090	0.60±0.04	1.19	-1.80	3.3±0.5	...
NGC6764	...	1.78	-1.79	...	...
NGC7250	0.22±0.05	0.77	-2.33	7.1±5.7	< 0.70 <sup>e</sup>
NGC7673	0.40±0.07	1.13	-2.07	2.9±0.7	...
NGC7714	0.41±0.03	2.31	-2.10	5.5±1.1	< 0.13
Mrk309	...	0.58	-1.76	...	...
Mrk542	...	0.36	-2.51	...	...

<sup>a</sup>Mean flux density at 2.18  $\mu$ m.

<sup>b</sup>Spectral slope of the NIR spectra.

<sup>c</sup>Line intensity ratio of [FeII] (1.257  $\mu$ m) to H<sub>2</sub> (2.121  $\mu$ m). The ratios are corrected for differential reddening, adopting the color excess values derived from Pa $\beta$ /Br $\gamma$  (CKS96).

<sup>d</sup>Line ratio of H<sub>2</sub>  $v = 1 - 0S(0)$  (2.223  $\mu$ m) to H<sub>2</sub>  $v = 1 - 0S(1)$  (2.121  $\mu$ m). The ratio has been determined for six galaxies only, due to limitations in wavelength coverage of the K-band spectra.

<sup>e</sup>The H<sub>2</sub>(2.22  $\mu$ m) line in NGC4194 is detected at the 3  $\sigma$  level. The large value of the upper limit in NGC7250 is due to the low signal-to-noise ratio of the spectrum beyond 2.2  $\mu$ m.



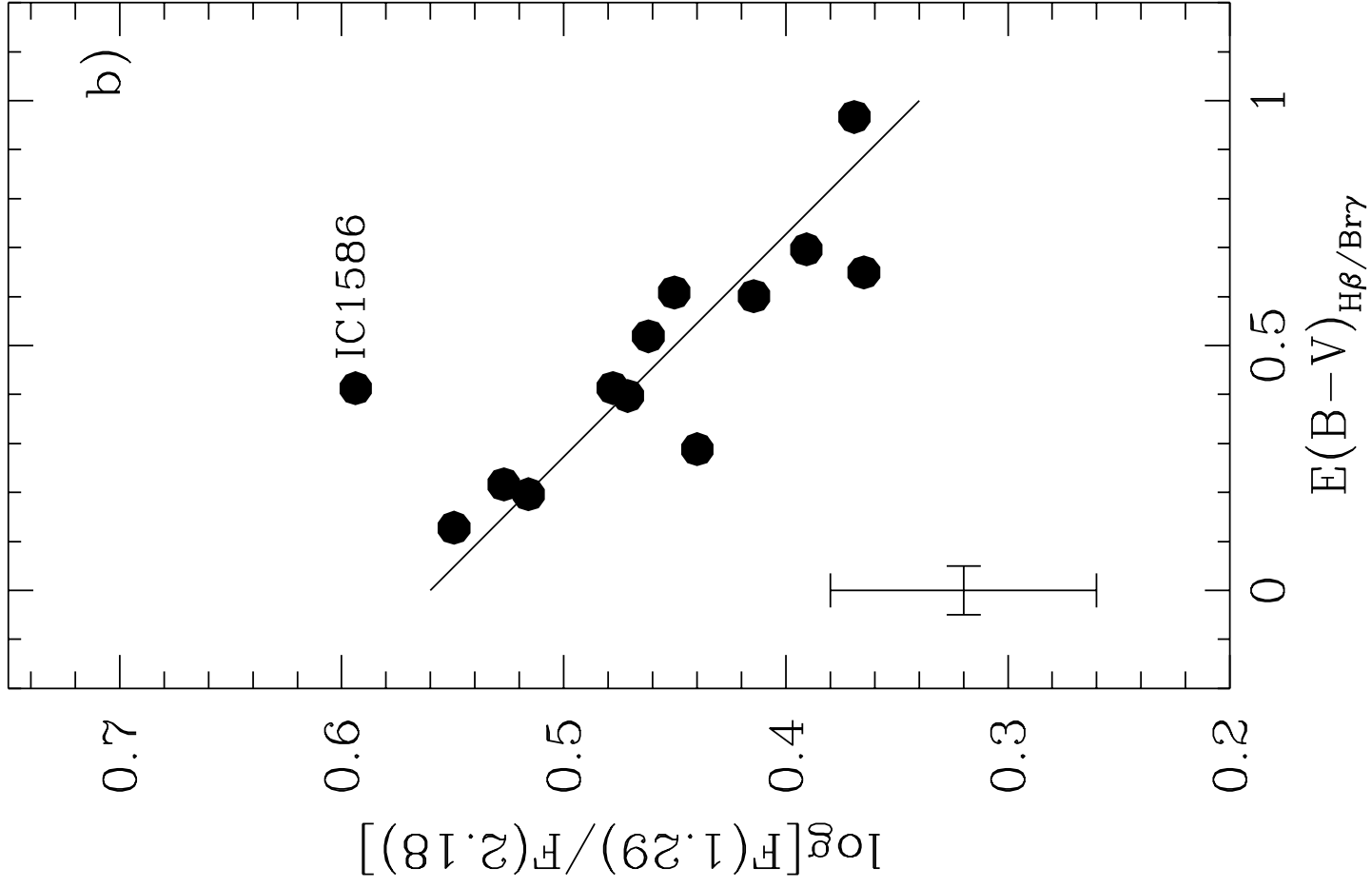
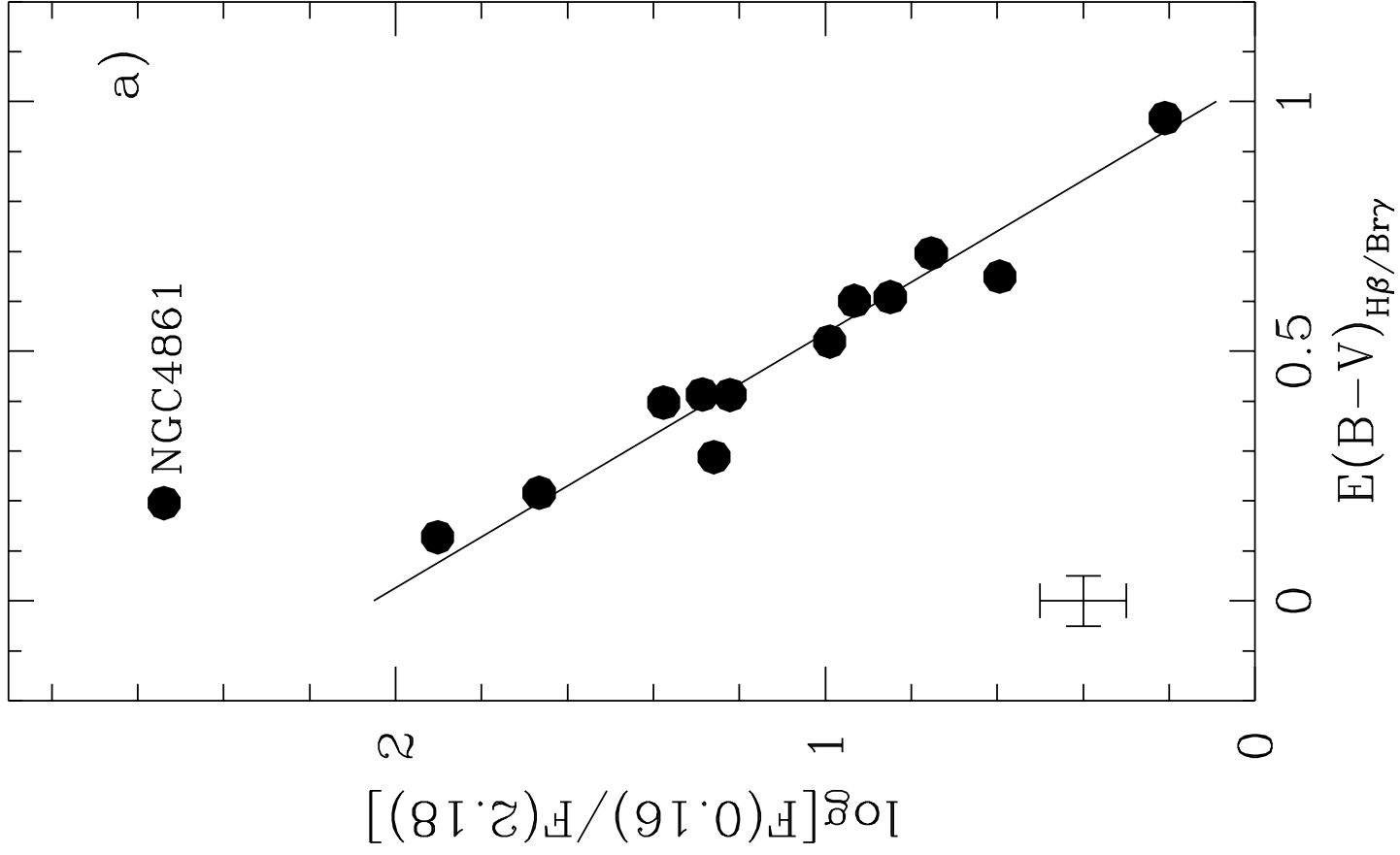


TABLE 5  
SELECTIVE OBSCURATION AND ZERO-REDDENING FLUX RATIOS

	E(B-V) $H\alpha/H\beta$	# Points in Fit	$\chi^2$ <sup>c</sup>	E(B-V) $H\beta/Br\gamma$	# Points in Fit	$\chi^2$ <sup>c</sup>
$k'(0.16)-k'(2.2)$ <sup>a</sup>	$4.03\pm0.40$	18	3.1	$4.90\pm0.38$	12	1.2
$k'(0.26)-k'(2.2)$ <sup>a</sup>	$3.33\pm0.60$	8	2.9	$5.00\pm0.69$	8	1.1
$k'(0.44)-k'(2.2)$ <sup>a</sup>	$2.20\pm0.35$	17	2.6	$3.15\pm0.38$	11	1.2
$k'(0.55)-k'(2.2)$ <sup>a</sup>	$1.70\pm0.30$	18	1.9	$2.47\pm0.30$	12	1.0
$k'(0.70)-k'(2.2)$ <sup>a</sup>	$1.22\pm0.30$	18	1.9	$1.90\pm0.30$	12	1.0
$k'(1.25)-k'(2.2)$ <sup>a</sup>	$0.43\pm0.15$	19	3.5	$0.55\pm0.10$	12	0.9
$k'(1.65)-k'(2.2)$ <sup>a</sup>	$0.19\pm0.09$	19	3.0	...	...	
$\log F(0.16)/F(2.2)$ <sup>b</sup>	$1.92\pm0.08$	18		$2.05\pm0.08$	12	
$\log F(0.26)/F(2.2)$ <sup>b</sup>	$1.65\pm0.11$	8		$1.83\pm0.11$	8	
$\log F(0.44)/F(2.2)$ <sup>b</sup>	$1.39\pm0.07$	17		$1.52\pm0.08$	11	
$\log F(0.55)/F(2.2)$ <sup>b</sup>	$1.21\pm0.07$	18		$1.31\pm0.07$	12	
$\log F(0.70)/F(2.2)$ <sup>b</sup>	$1.06\pm0.08$	18		$1.14\pm0.08$	12	
$\log F(1.25)/F(2.2)$ <sup>b</sup>	$0.55\pm0.06$	19		$0.56\pm0.05$	12	
$\log F(1.65)/F(2.2)$ <sup>b</sup>	$0.38\pm0.05$	19		...	...	

<sup>a</sup>The selective obscuration  $k(\lambda_1)-k(\lambda_2)$  for the starbursts' stellar continuum. The wavelengths  $\lambda_1$  and  $\lambda_2$  are in units of  $\mu\text{m}$ .

<sup>b</sup>The reddening-free stellar continuum flux ratio.

<sup>c</sup>Reduced  $\chi^2$ .

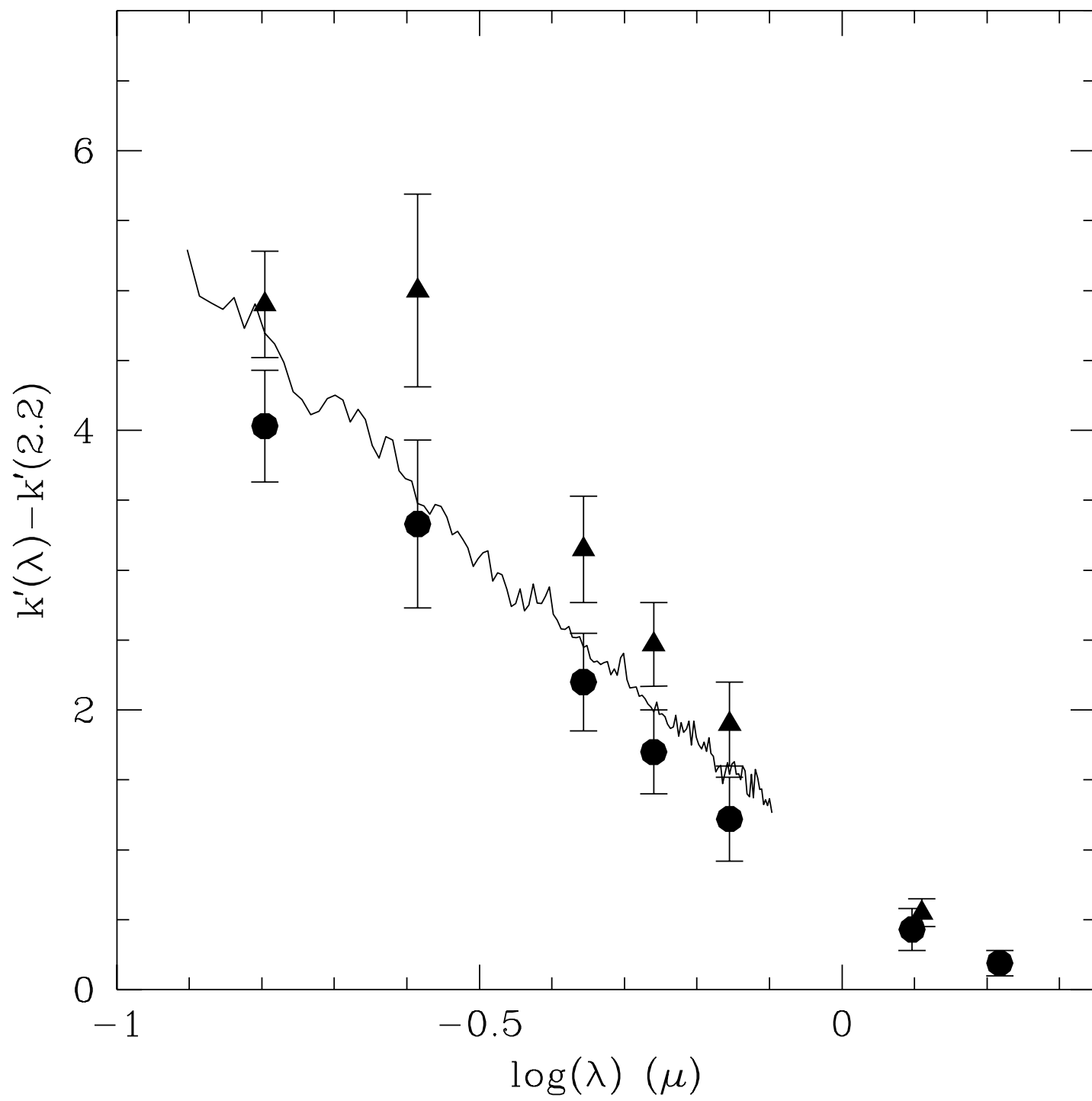


TABLE 6  
STAR FORMATION AND SUPERNOVA RATES

Galaxy	$L_{[FeII]}^a$ $L_{\odot, bol}$	$snr([FeII])^b$ $yr^{-1}$	SFR100 <sup>c</sup> $M_{\odot} yr^{-1}$	SFR30 <sup>c</sup> $M_{\odot} yr^{-1}$	$snr100^b$ $yr^{-1}$	$snr30^b$ $yr^{-1}$
IC1586	6.23E+06	0.094	6.4	27.6	0.036	0.157
Haro15 <sup>d</sup>	...	...	4.4	19.1	0.025	0.109
Mrk357 <sup>d</sup>	...	...	31.1	134.8	0.177	0.768
IC214	3.03E+07	0.459	28.5	123.8	0.163	0.706
NGC1140 <sup>d</sup>	...	...	1.4	6.0	0.008	0.034
NGC1569	2.88E+03	<0.001	<0.1	0.2	<0.001	0.001
NGC1614	8.05E+07	1.218	90.8	394.0	0.517	2.246
NGC4194	1.13E+07	0.171	14.1	61.1	0.080	0.348
NGC4385	3.35E+06	0.051	5.2	22.4	0.029	0.128
NGC4861	2.59E+04	<0.001	0.9	3.7	0.005	0.021
NGC5860	3.40E+06	0.051	8.1	35.1	0.046	0.200
NGC6052	3.32E+06	0.050	7.2	31.4	0.041	0.179
NGC6090	2.76E+07	0.418	55.3	239.9	0.315	1.367
NGC6217 <sup>d</sup>	...	...	0.2	0.7	0.001	0.004
NGC7250	2.93E+05	0.004	0.5	2.1	0.003	0.012
NGC7673	2.89E+06	0.044	4.3	18.5	0.024	0.105
NGC7714	2.99E+06	0.045	6.3	27.4	0.036	0.156
Mrk309 <sup>d</sup>	...	...	15.4	66.7	0.088	0.380
Mrk542 <sup>d</sup>	...	...	3.1	13.5	0.018	0.077

<sup>a</sup>Luminosity of the  $[FeII](1.257 \mu m)$  emission line, corrected for both foreground Galactic reddening and intrinsic reddening using the value for the color excess from the  $H\beta/Br\gamma$  ratio.

<sup>b</sup>The current supernova rate,  $snr([FeII])$ , as derived from the iron luminosity, see Equation (8); the predicted supernova rates,  $snr100$  and  $snr30$ , as derived from Equation (10) using the star formation rates SFR100 and SFR30, respectively.

<sup>c</sup>Star Formation Rates. SFR100 is derived from Equation (9a) adopting an upper mass limit of  $100 M_{\odot}$  to the IMF. SFR30 adopts as an upper limit  $30 M_{\odot}$ , see Equation (9b).

<sup>d</sup>The star formation rates and the supernova rates are derived from the reddening corrected  $H\alpha$  line flux, using Equations (8) and (9) and the relation  $f(H\alpha)=97.5 \times f(Br\gamma)$ .

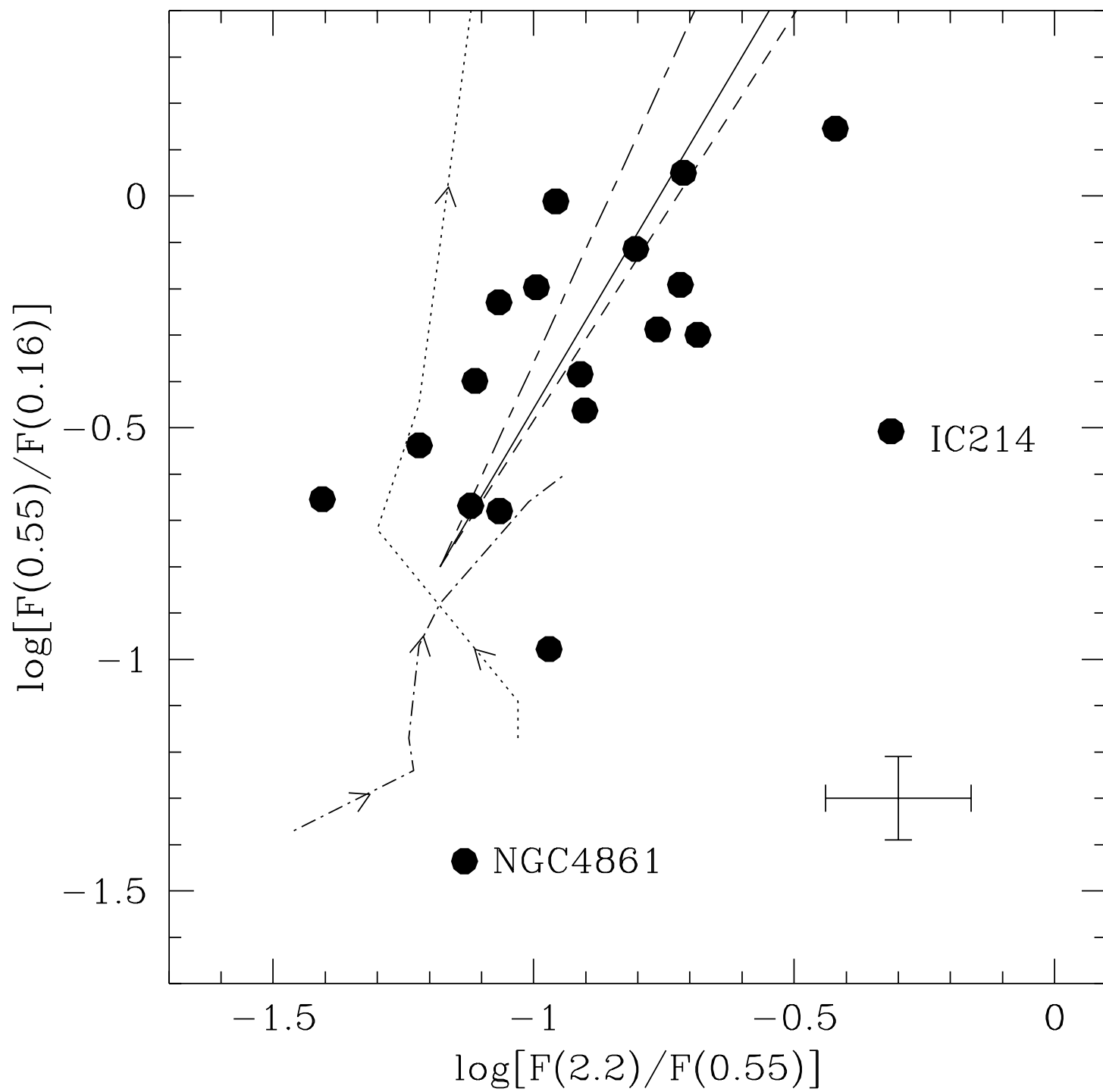


TABLE 7  
MEASURED AND PREDICTED EQUIVALENT WIDTHS

Spectrum <sup>a</sup>	EW(H $\alpha$ ) ( $\text{\AA}$ )	EW(Pa $\beta$ ) ( $\text{\AA}$ )	EW(Br $\gamma$ ) ( $\text{\AA}$ )
Template Starburst Spectrum (TSS)	100.	18.	14.
Model Spectrum ( $2 \times 10^7$ yr)	129.	21.	14.
NGC 7714	238.	29.	22.
Model Spectrum ( $1 \times 10^7$ yr)	205.	40.	24.
NGC 4861	1060.	199.	123.
Model Spectrum 1 ( $4 \times 10^6$ yr) <sup>b</sup>	1690.	410.	240.
Model Spectrum 2 ( $3 \times 10^6$ yr) <sup>b</sup>	1310.	300.	150.

<sup>a</sup>Galaxy Spectra from which the equivalent widths of the hydrogen lines are being measured or predicted. Each galaxy is coupled with the model which provides the best fit to the observed spectrum. In parentheses the age of the star-forming population which enters in the model SED is given. For each galaxy and for the template starburst spectrum, the first row shows the observed EW values, after correction for the effects of differential reddening between line and continuum (see text). The second row shows the values obtained from the model(s).

<sup>b</sup>For NGC 4861, two best fitting composite populations are reported, differing only for the nature of the star-forming population, which is a  $4 \times 10^6$  yr population undergoing constant SF in model 1, and is a  $3 \times 10^6$  yr population originated from an instantaneous burst in model 2.

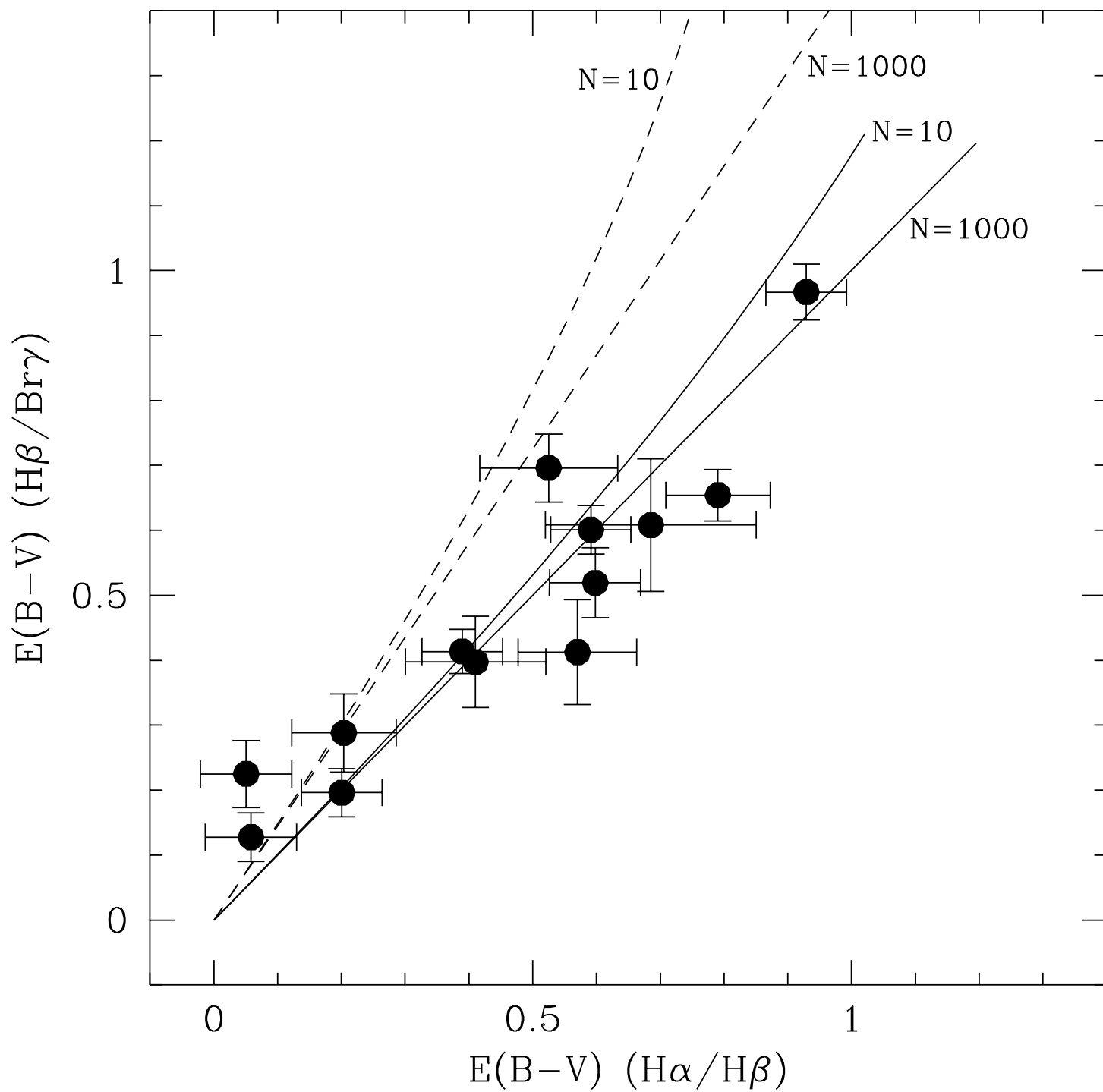


TABLE 8  
GALAXIES MASS AND LUMINOSITY

Galaxy	M(HI) <sup>a</sup> 10 <sup>9</sup> M <sub>⊙</sub>	v(HI) <sup>b</sup> km/s	t <sub>100</sub> <sup>c</sup> 10 <sup>9</sup> yr	M <sub>d</sub> <sup>d</sup> 10 <sup>9</sup> M <sub>⊙</sub>	M(HI)-ap <sup>e</sup> 10 <sup>9</sup> M <sub>⊙</sub>	L <sub>K</sub> /SFR100 <sup>f</sup> 10 <sup>9</sup> L <sub>K,⊙</sub> /M <sub>⊙</sub> yr <sup>-1</sup>	M <sub>d</sub> /L <sub>K</sub> <sup>g</sup> M <sub>⊙</sub> /L <sub>K,⊙</sub>
IC1586	7	200.	1.1	38.4	3.96	5.34	1.13
Haro15	13	220.	2.9	49.5	1.22	7.50	1.50
Mrk357	19	280.	0.6	159.1	19.00	2.79	2.14
IC214	30	420.	1.1	261.0	4.78	10.48	0.87
NGC1140	9	218.	6.3	11.3	0.26	3.17	2.54
NGC1569	0.1	90.	>1.0	0.2	0.001	>1.73	0.92
NGC1614	10	290.	0.1	72.6	0.40	4.00	0.20
NGC4194	5	200.	0.3	17.5	0.12	5.20	0.24
NGC4385	3	120.	0.6	5.6	0.05	4.73	0.23
NGC4861	4	120.	4.1	2.2	0.02	0.55	4.29
NGC5860	...	...	...	...	...	8.14	...
NGC6052	12	440.	1.7	134.0	1.15	5.00	3.73
NGC6090	12	350.	0.2	154.3	1.94	3.38	0.83
NGC6217	13	250.	65.0	14.1	0.09	66.18	1.06
NGC7250	1	228.	2.0	10.2	0.03	5.27	3.87
NGC7673	9	202.	2.1	21.7	0.32	6.05	0.84
NGC7714	7	260.	1.1	20.8	0.13	3.00	1.10
Mrk309	8	215.	0.5	76.4	2.73	9.32	0.53
Mrk542	...	...	...	...	...	11.75	...

<sup>a</sup>The total HI mass, as derived from the RC3 (de Vaucouleurs et al. 1991).

<sup>b</sup>The HI velocity width, from the compilation of Huchtmeier & Richter (1989).

<sup>c</sup>Time required to consume the HI gas supply if the star formation rate SFR100 remains constant.

<sup>d</sup>The dynamical mass contained within the observational aperture, as derived from the HI velocity.

<sup>e</sup>The HI mass contained within the observational aperture.

<sup>f</sup>The K-band luminosity contained within the observational aperture, per unit of star formation rate, after correction for intrinsic reddening. The luminosity is in units of the K-band solar luminosity, L<sub>K,⊙</sub>=2.297E+28 erg/s/Å (Colina, Bohlin, & Castelli 1996).

<sup>g</sup>The mass-to-light ratio from the dynamical mass and the K-band luminosity.



